

# Unifying Multiple Foundation Models for Advanced Computational Pathology

Wenhui Lei<sup>1,2‡</sup>, Yusheng Tan<sup>3‡</sup>, Anqi Li<sup>3‡</sup>, Hanyu Chen<sup>4‡</sup>, Hengrui Tian<sup>1</sup>, Ruiying Li<sup>5</sup>, Zhengqun Jiang<sup>1</sup>, Fang Yan<sup>2</sup>, Xiaofan Zhang<sup>\*1,2</sup>, Shaoting Zhang<sup>\*1,2</sup>

<sup>1</sup>*Shanghai Jiaotong University, Shanghai, China*

<sup>2</sup>*Shanghai Artificial Intelligence Laboratory, Shanghai, China*

<sup>3</sup>*Washington University in St. Louis, St. Louis, USA*

<sup>4</sup>*The First Hospital of China Medical University, Shenyang, China*

<sup>5</sup>*University of Science and Technology Beijing, Beijing, China*

‡ Contributed Equally

**\*Corresponding author:** Xiaofan Zhang ([xiaofan.zhang@sjtu.edu.cn](mailto:xiaofan.zhang@sjtu.edu.cn)), Shaoting Zhang ([shaoting.zhang@sjtu.edu.cn](mailto:shaoting.zhang@sjtu.edu.cn))

**Foundation models have advanced computational pathology by learning transferable visual representations from large histological datasets, yet recent evaluations reveal substantial variability in their performance across tasks. This inconsistency arises from differences in training data diversity and is further constrained by the reliance of many high-performing models on proprietary datasets that cannot be shared or expanded. Offline distillation offers a partial remedy but depends heavily on the size and heterogeneity of the distillation corpus and requires full retraining to incorporate new models. To address these limitations, we propose Shazam, a task-specific online integration framework that unifies multiple pretrained pathology foundation models within a single flexible inference system. Shazam fuses multi-level representations through adaptive expert weighting and learns task-aligned features via online distillation. Across spatial transcriptomics prediction, survival prognosis, tile classification, and visual question answering, Shazam consistently outperforms strong individual models, highlighting its promise as a scalable approach for harnessing the rapid evolution of pathology foundation models in a unified and adaptable manner.**

# Introduction

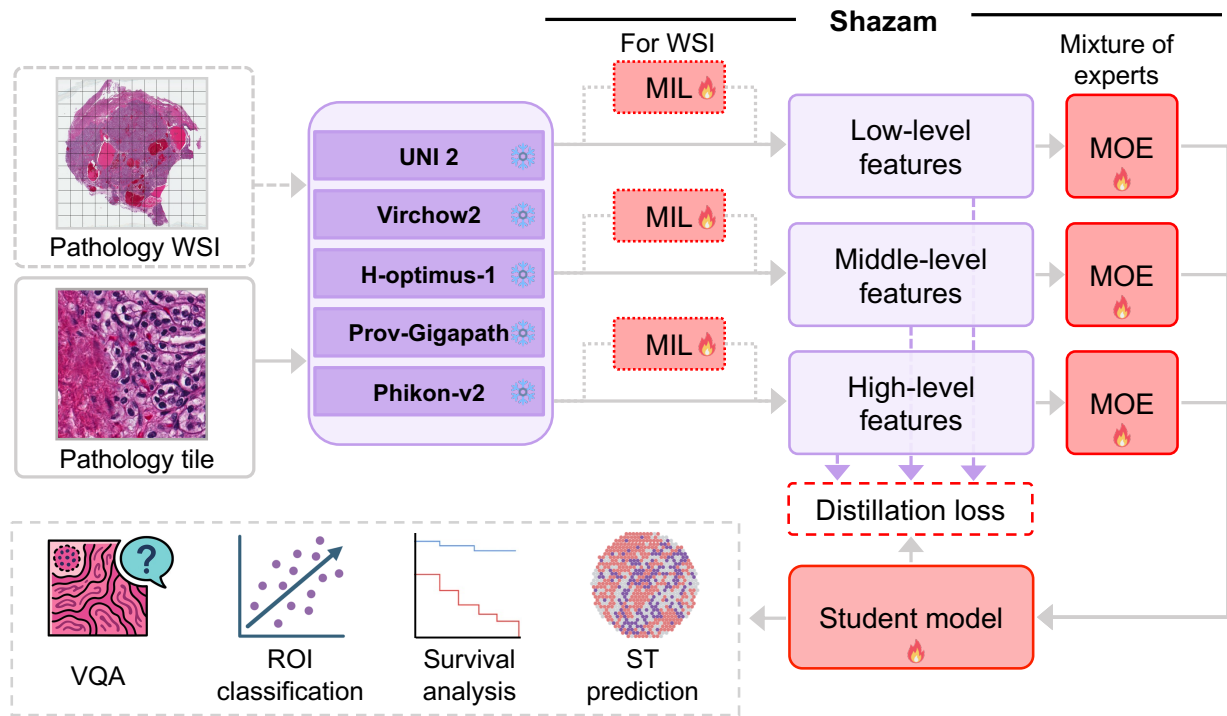
Histopathology remains the cornerstone of cancer diagnosis and treatment planning, providing direct visualization of tissue architecture, cellular morphology, and tumor–microenvironment interactions that guide clinical decision-making. Advances in whole-slide imaging (WSI) have transformed this traditionally microscope-based discipline into a scalable digital workflow, enabling the systematic capture, storage, and analysis of gigapixel-resolution slides. This digital transition has laid the foundation for modern computational pathology (CPath), where artificial intelligence systems can interrogate WSI data to support diagnostic, predictive, and prognostic tasks<sup>1,2</sup>. Building on this momentum, recent pathology foundation models have introduced a new paradigm for CPath. By pretraining on millions of tiles extracted from large cohorts of WSIs across diverse organs and cancer types, models such as Virchow<sup>3</sup>, UNI<sup>4</sup>, and H-Optimus-1<sup>5</sup> learn broad and transferable representations that enhance data efficiency and improve downstream performance across a wide spectrum of clinical tasks.

Despite these advances, recent benchmarking studies have revealed substantial performance variability among pathology foundation models across tasks<sup>6–8</sup>. Much of this inconsistency reflects differences in the scale, diversity, and institutional origins of the pretraining data, and no single model consistently performs well across diagnostic, prognostic, molecular, and region-level tasks. Compounding this challenge, many high-performing models rely on large proprietary datasets that cannot be shared due to privacy and institutional constraints<sup>4,5,9</sup>. This lack of data accessibility prevents the research community from steadily expanding the pretraining corpus over time, constraining the growth in data diversity that has supported advances in natural image and language foundation models<sup>10–12</sup>.

To address the challenges posed by inaccessible training data, recent work has explored combining existing foundation models through offline knowledge distillation, exemplified by GPFM<sup>13</sup>. In this framework, multiple pretrained teacher models first generate features on a curated distillation dataset, and a student model is trained to learn from these signals through expert distillation, complemented by self-distillation that aligns local and global representations. While this strategy provides a practical means of integrating knowledge from several models, it faces several inherent limitations. First, because the distillation process is performed offline, incorporating newly developed foundation models requires retraining the student model from scratch, making rapid integration of emerging advances difficult. Second, the effectiveness of offline distillation depends heavily on the scale and diversity of the available distillation dataset, which in practice is restricted to publicly accessible or newly assembled collections. This constraint limits the range of morphologic and clinical variation that the student model can encounter during distillation, reducing its ability to fully capture the complementary behaviors of diverse teacher models<sup>14</sup>. Third, offline distillation provides limited flexibility for

task-specific adaptation, since the student model learns from teacher outputs generated in a task-agnostic manner and cannot selectively emphasize teacher knowledge that is particularly relevant for a specific downstream prediction target. These constraints highlight the need for an alternative strategy that can directly leverage multiple foundation models in a more flexible and adaptive way, without relying on repeated offline retraining or large-scale distillation corpora.

To address these challenges, we developed Shazam, a unified pathology foundation model that integrates multiple pretrained models within a single and flexible inference framework (Fig.1a). In contrast to offline distillation approaches that require assembling a dedicated distillation dataset and retraining a new model, Shazam performs task-specific online integration. It combines multi-level representations from diverse pathology foundation models through a lightweight Mixture-of-Experts (MoE)<sup>15</sup> mechanism and adapts the fusion process directly to the target task. This design enables Shazam to extract the most informative elements from each model without the need to restart pretraining or construct large-scale distillation corpora whenever new foundation models become available. We evaluate Shazam across a wide range of downstream applications, including spatial transcriptomics prediction, whole-slide survival prognosis, tile-level classification, and visual question answering. These tasks span molecular, regional, and slide-level endpoints and together reflect the breadth of clinical challenges encountered in computational pathology. Across these evaluations, Shazam demonstrates consistent and robust performance. In total, it achieves an average ranking score of 1.17 across 30 benchmarks, substantially outperforming the second-best model, Virchow2, which attains an average of 3.20. The results show that flexible online integration of existing foundation models can effectively consolidate their complementary strengths and provide a practical route toward more adaptable and widely applicable computational pathology systems.

**a.****b.**

	ST prediction										Survival analysis										Tile classification	
Shazam	1	1	1	1	1	1	1	1	1	3	1	1	1	1	1	1	2	1	2	1	1	1
UNI 2	2	4	4	2	6	3	5	4	3	5	5	4	5	5	4	5	5	4	3	4	2	4
Virchow2	5	5	3	3	2	5	6	2	5	6	2	3	4	3	2	3	3	2	2	5	1	2
H-optimus-1	3	2	2	4	5	6	2	6	2	3	1	2	2	2	5	2	2	3	1	5	3	3
Prov-Gigapath	6	6	6	6	3	4	4	3	6	4	4	5	3	4	4	6	5	6	6	4	3	5
Phikon-v2	4	3	5	5	4	2	3	5	4	2	6	6	6	6	4	6	5	6	4	6	6	6
	HEST-BRE	HEST-PR	HEST-SK	HEST-BO	HEST-LI	HEST-KI	HEST-BRA	HEST-BL	TCGA-BLCA	TCGA-CESC	TCGA-COAD	TCGA-GBMLGG	TCGA-KIRC	TCGA-LUAD	TCGA-SKCM	TCGA-STAD	PanCancer-TCGA	chaoyang	BACH	CCRCC-TCGA-HEI	PCAM	UniTopatho
																					CRC-100K	HunCRC
																						PathVCA
																						Average Rank

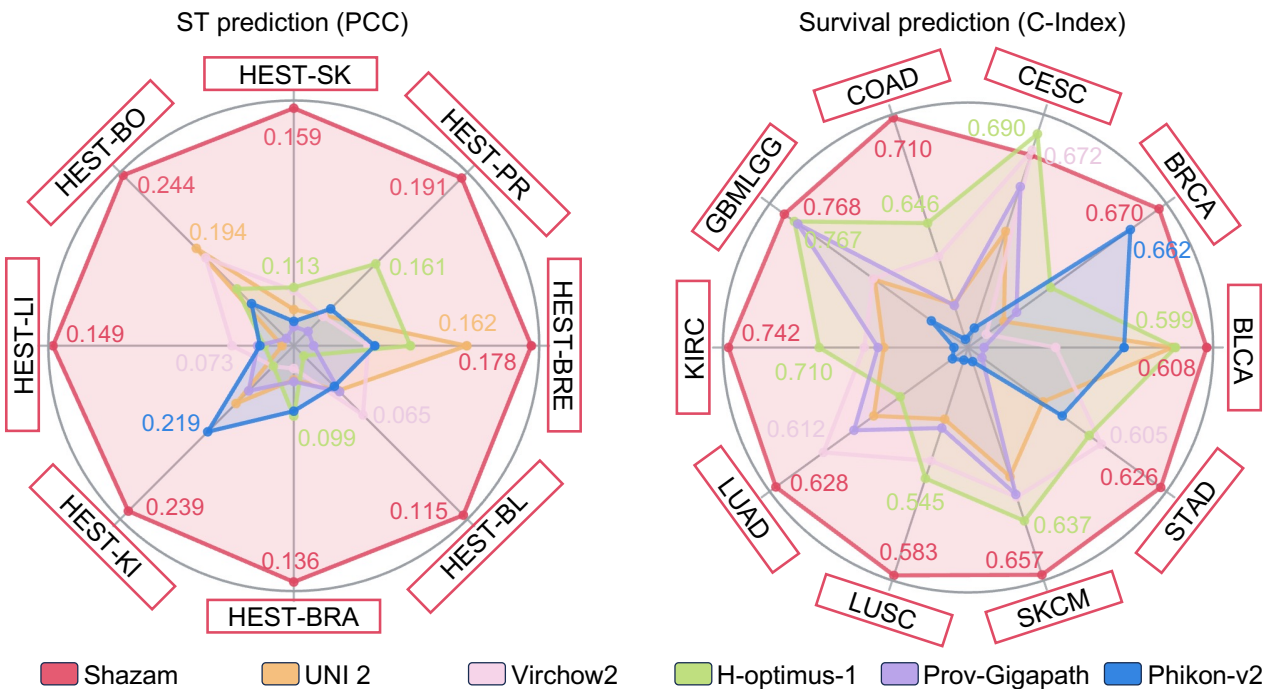
**c.**

Figure 1: **a**, Overview of the Shazam framework. Multiple pretrained pathology foundation models are used to extract features from WSIs and tiles. For WSI-level tasks, each model first produces slide representations through a multiple-instance-learning module, whereas tile-level tasks directly use tile embeddings. Shazam performs task-specific online feature integration by fusing low-, middle-, and high-level features and assigning adaptive mixture-of-experts weights. A student model is optimized with an online distillation objective to learn cohesive task-aligned representations without the need for offline distillation or retraining. **b**, Overall ranking of Shazam and baseline foundation models across 30 downstream benchmarks. A lower rank indicates stronger performance, with a rank of 1 assigned to the top-performing model for each task. Shazam attains the best mean ranking and ranks first on 26 of the 30 tasks. **c**, Comparison of model performance in spatial transcriptomics and survival prediction measured by PCC and C-index.

## Results

Shazam is built upon five state-of-the-art pathology foundation models, including UNI 2<sup>4</sup>, Virchow2<sup>16</sup>, H-optimus-1<sup>5</sup>, Prov-Gigapath<sup>9</sup>, and Phikon-v2<sup>17</sup>, and is evaluated across a broad spectrum of downstream applications. Our benchmark covers four major task categories: spatial transcriptomics prediction with eight tasks, whole-slide survival analysis with ten tasks, tile-level classification with eleven tasks, and pathology visual question answering. The overall ranking across all thirty tasks is summarized in Fig. 1b. Shazam achieves the strongest average ranking score of 1.17 and ranks first on 26 of the 30 tasks. By comparison, the next best model, Virchow2, attains an average ranking score of 3.20 and leads only 2 tasks. These findings demonstrate that Shazam substantially outperforms the foundation models on which it is built and exhibits strong generalization across diverse molecular, regional, and slide-level prediction settings.

### 1 Shazam enhances spatial transcriptomic prediction

Spatial transcriptomics (ST) provides high-resolution maps of gene expression that reveal the molecular architecture of tissues and the tumor microenvironment, offering insights beyond what morphology alone can capture<sup>18–20</sup>. However, the high cost of ST assays and the limited availability of standardized paired H&E–ST datasets have traditionally restricted most computational analyses to narrow tasks and small patient cohorts<sup>21–23</sup>. Leveraging pathology foundation models to infer spatial gene expression directly from H&E images offers a scalable alternative, enabling the discovery of treatment-relevant biomarkers across much larger datasets. To assess performance on this challenging task, we compared Shazam against a suite of strong pathology foundation-model baselines for predicting spatial gene expression from H&E slides in the HEST-1K dataset<sup>24</sup>, focusing on clinically actionable genes as prediction targets. We considered eight organ-specific cohorts with sufficient paired data, including bowel, liver, breast, prostate, skin, brain, kidney, and bladder, and curated clinically actionable gene sets for each cohort. Additional details are provided in Methods and Supplementary Table1.

For each cohort, we followed the patient-level splitting strategy and conducted patient-level  $K$ -fold cross-validation, formulating gene expression inference as a tile-level regression task (details in Methods). For each baseline foundation model, we attached a multilayer perceptron to its pretrained representations to predict log-

normalized spot-level gene expression. Shazam adopted the same regression setting but first integrated representations from multiple foundation models into a unified feature space before prediction with the multilayer perceptron. We quantified performance using the Pearson Correlation Coefficient (PCC) between predicted and measured spot-level expression profiles, consistent with the evaluation protocol of HEST-1K as described in Methods.

Across all eight organ types, Shazam consistently achieved the highest PCCs, with an average improvement of 0.08–0.17 over the strongest individual foundation models (Fig. 2a). The baseline models exhibit clear organ-dependent variability, with Virchow2 performing relatively well in brain and skin cancers, H-optimus-1 showing stronger results in prostate and bladder cancers, and UNI 2 occasionally ranking higher in bowel or kidney cancers (details in Supplementary Tables 2,3). These differences indicate that existing pathology foundation models often reflect the tissue compositions and morphological patterns emphasized during pretraining, which makes it challenging for a single model to maintain uniformly strong performance across distinct organs. In contrast, Shazam ranks first in all eight cancer types, achieving an average ranking of 1.0 and significantly outperforming the next-best models, including UNI 2, Virchow2, and H-optimus-1, whose mean ranking scores are approximately 3.25 ( $p=0.004$ ). This consistent advantage across glandular, stromal-rich, and neuroepithelial tissues reflects Shazam’s ability to integrate complementary representations from multiple expert models and to provide stable, cross-organ generalization.

Consistent with these quantitative results, Fig. 2b shows a representative bowel cancer case from the HEST-1K dataset. Shazam accurately captured the heterogeneous spatial pattern of IDH1 expression, including the pronounced up-regulation in dysplastic tumor glands relative to adjacent normal glandular epithelium. This tumor-specific elevation is clearly reflected in the ground truth and was faithfully reproduced only by Shazam, whereas baseline models such as UNI 2, Virchow2, H-optimus-1, GigaPath, and Phikon-v2 either failed to distinguish these compartments or produced the opposite trend. Shazam also recovered the expected low-expression domains within stromal and muscular layers, which other models tended to oversmooth or underrepresent. These results illustrate Shazam’s ability to align tissue morphology with gene-level variation, capturing both tumor-associated up-regulation and stromal or muscular down-regulation patterns that single-model architectures frequently mislocalize.

Collectively, these results demonstrate that Shazam effectively learns a unified morphomolecular representation, translating histological features into gene-level spatial expression patterns with superior accuracy and cross-tissue generalization. Taken together, these findings show that Shazam provides a practical and reliable framework for spatial transcriptomic prediction, offering a flexible foundation for downstream molecular analysis without overreliance on costly assays.

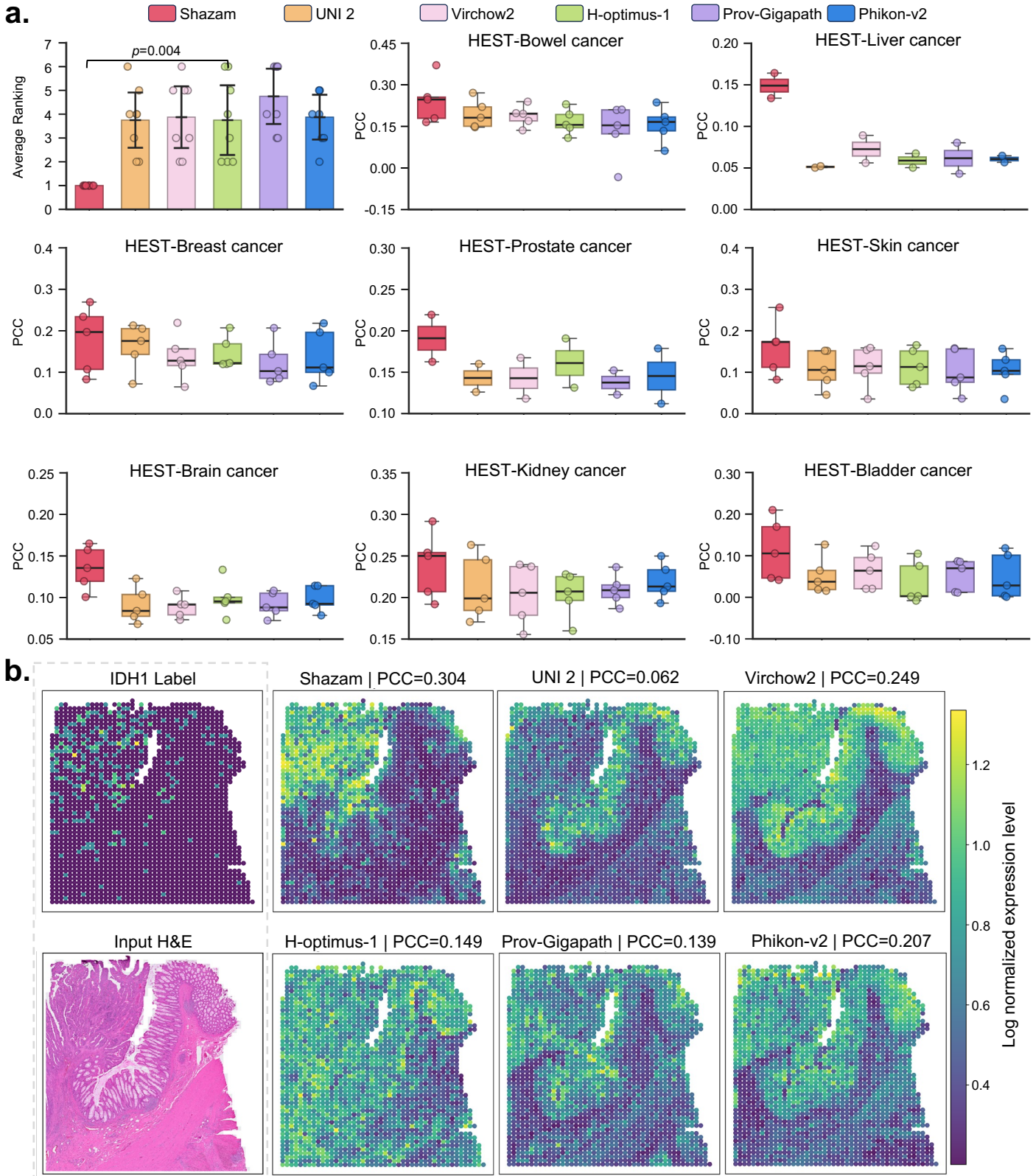


Figure 2: **a.** Quantitative comparison of prediction accuracy across eight organ types in the HEST-1k dataset, measured by Pearson Correlation Coefficient (PCC). Shazam consistently outperforms existing pathology foundation models (UNI 2, Virchow2, H-optimus-1, Phikon-v2, GigaPath). **b.** Spatial prediction of IDH1 expression in a colorectal cancer sample. Shazam accurately recapitulates the elevated expression within dysplastic tumor glands and the reduced expression in stromal and muscular layers, aligning closely with the measured spatial transcriptomic profile. Baseline models fail to recover these tissue-compartment differences.

## 2 Shazam advances survival prognosis

Accurate survival prognosis is central to cancer management, guiding treatment selection, surveillance strategies, and clinical trial allocation<sup>25</sup>. Yet substantial variability in patient outcomes persists even within the same cancer type, underscoring the limitations of existing clinical and genomic biomarkers. Histopathology, obtained routinely at diagnosis and rich in biological information, remains an underleveraged resource for prognostic modeling. To assess whether Shazam’s unified morphomolecular representations can capture outcome-relevant signals, we conducted a pan-cancer evaluation across ten The Cancer Genome Atlas Program (TCGA)<sup>26</sup> cohorts. For each cohort, diagnostic whole-slide images were processed to obtain slide-level representations using attention-based multiple instance learning (details in Methods), and Cox proportional hazards models were trained in a five-fold patient-level cross-validation framework to evaluate the generalizability of survival predictions derived directly from H&E slides.

Across the ten cancer types, Shazam achieved the strongest overall prognostic performance, attaining a mean C-Index of 0.666 (Supplementary Tables 4-6). This surpasses the best-performing individual foundation model, H-optimus-1 (0.642), and exceeds the average performance of Virchow2 (0.631), Prov-GigaPath (0.617), UNI 2 (0.617), and Phikon-v2 (0.594). A paired Wilcoxon signed-rank test confirmed that Shazam’s improvement over H-optimus-1 is statistically significant ( $p = 0.007$ ), indicating a consistent advantage rather than cohort-specific variability. Shazam delivered noticeable gains in several cancer types with heterogeneous histology, including colon adenocarcinoma (COAD), where the C-Index increased from 0.646 (H-optimus-1) to 0.710, and lung squamous cell carcinoma (LUSC), where it rose from 0.545 (H-optimus-1) to 0.583. These improvements highlight Shazam’s capacity to integrate complementary strengths from multiple foundation models, yielding a more comprehensive and discriminative representation of disease progression than any individual model.

To further evaluate the clinical relevance of these quantitative gains, we performed Kaplan–Meier analyses using Shazam-derived risk scores. Patients were stratified into high-risk and low-risk groups using a median cutoff. As shown in Fig. 3b, Shazam produced clear and statistically significant separation between survival curves in nine of the ten cancer types (two-sided log-rank test,  $p < 0.05$  in all except CESC). The pronounced divergence between the high- and low-risk groups is consistent with Shazam’s elevated C-Index values and demonstrates its ability to extract outcome-relevant morphologic features from routine histology. These findings collectively show that Shazam’s unified representations not only improve quantitative survival prediction but also support robust patient stratification across diverse cancer types, underscoring its potential value for downstream clinical decision support<sup>27</sup>.

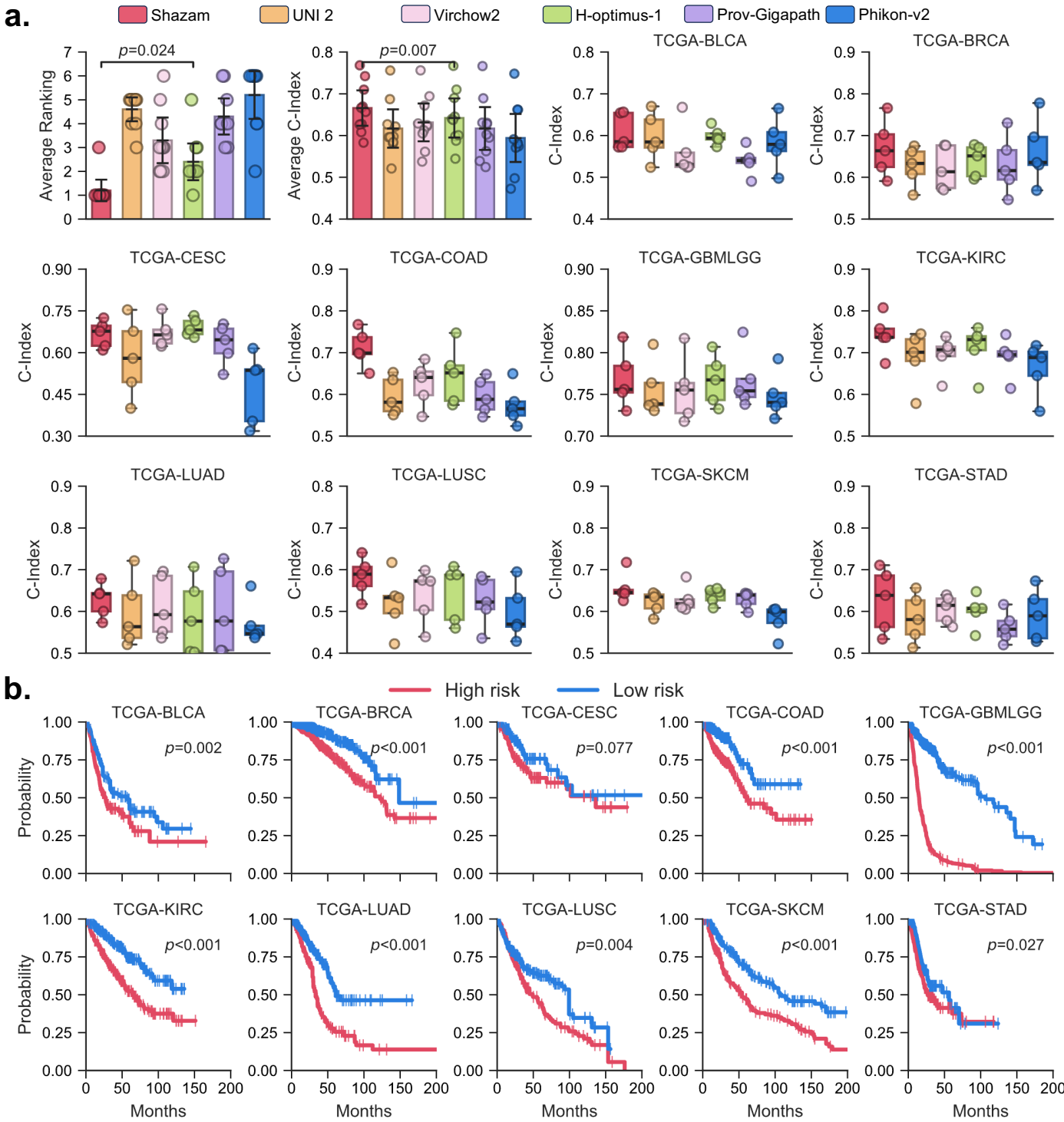


Figure 3: **a**, C-Index comparison of Shazam and baseline pathology foundation models across multiple cancer cohorts. Shazam consistently outperforms all baselines except in TCGA-CESC, reflecting its enhanced ability to derive prognostic features from histology. **b**, Kaplan–Meier curves for a representative cohort, showing significant separation between high-risk and low-risk groups predicted by Shazam (two-sided log-rank test,  $p < 0.05$ ), except the TCGA-CESC. The observed survival differences highlight the Shazam’s capacity to recover clinically meaningful prognostic information from whole-slide images.

### 3 Shazam improves tile-level performance across diverse histopathology tasks

Tile-level tasks provide a stringent assessment of a model’s capacity to capture fine-grained morphological patterns, local microenvironmental variation, and institution- or stain-specific distribution shifts, all of

which are typically underrepresented in whole-slide aggregation benchmarks. Rather than relying on a single foundation model and its fixed inductive biases, Shazam integrates multi-scale features from several complementary pathology foundation models and adaptively selects informative channels at inference time. This produces tile-level descriptors that reflect a coordinated ensemble of morphological primitives with greater flexibility across heterogeneous tissue contexts. To systematically evaluate this integrative design, we benchmarked Shazam across eleven diverse tile-level datasets: HunCRC for colorectal tissue classification<sup>28</sup>, UniToPatho for colorectal polyp grading<sup>29</sup>, PCAM<sup>30</sup> for metastatic detection, ESCA for esophageal carcinoma subtyping<sup>31</sup>, PanCancer-TIL for tumor-infiltrating lymphocytes assessment<sup>32</sup>, CCRCC-TCGA-HEL<sup>33</sup> for renal carcinoma tissue classification, BACH for breast cancer categorization<sup>34</sup>, CRC-MSI for microsatellite instability screening<sup>35</sup>, PanCancer-TCGA for pan-cancer tissue classification<sup>36</sup>, and Chaoyang for colon pathology<sup>37</sup>. These datasets span a wide range of tasks and clinical settings, providing a comprehensive evaluation of Shazam’s tile-level generalizability.

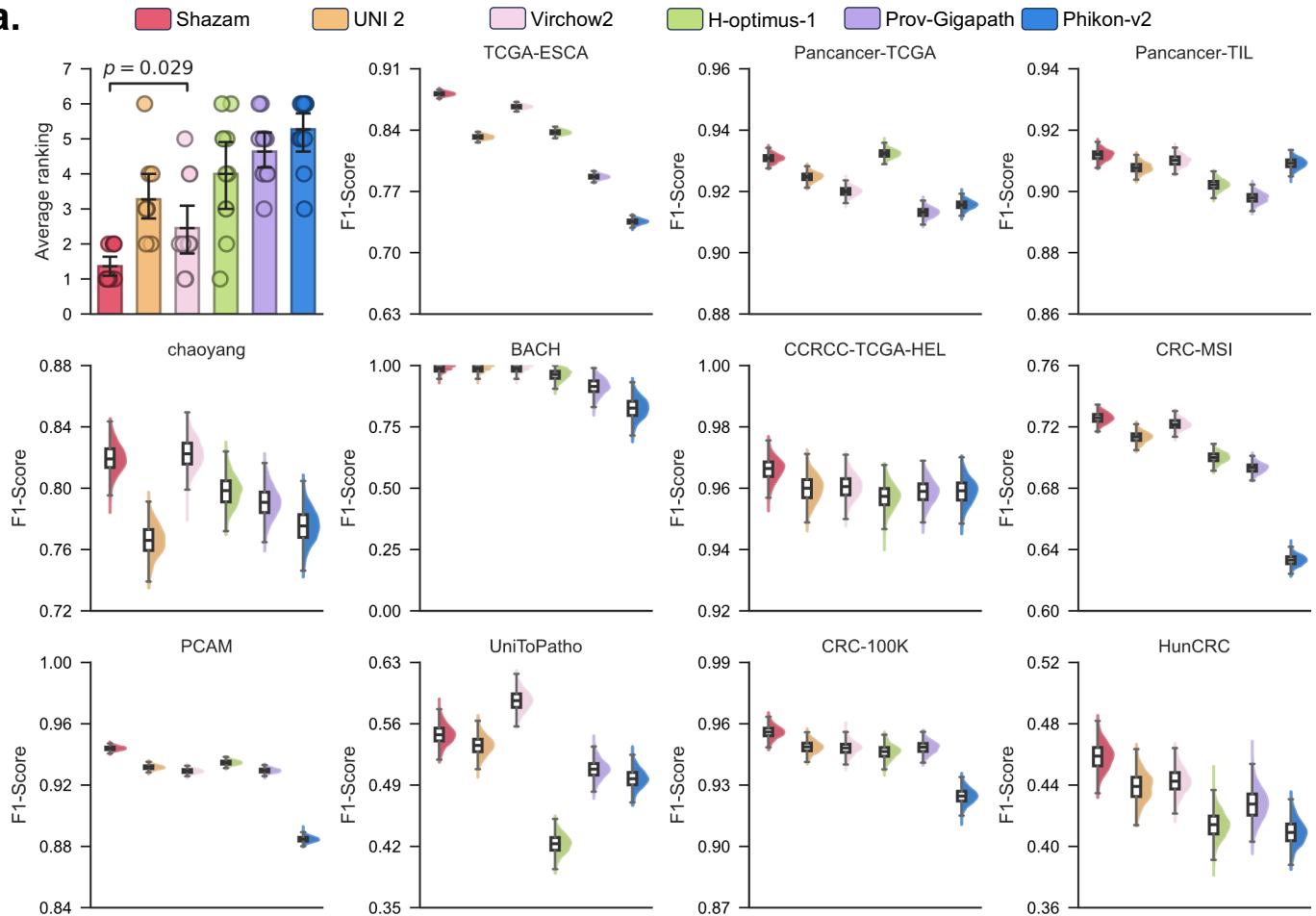
Across the eleven tile-level benchmarks, Shazam achieved the strongest overall performance, with a mean ranking score of 1.36 compared with 2.46 for the strongest baseline, Virchow2, underscoring the consistent advantage of its integrative multi-model formulation (Supplementary Tables 7-17). Shazam delivered the highest F1 score on several representative datasets. On PCAM, it achieved 0.914 and surpassed Virchow2 by approximately 1.4%. On PanCancer-TIL, Shazam reached 0.852, outperforming Virchow2 by about 1.0%. On PanCancer-TCGA, it attained 0.844, exceeding H-optimus-1 at 0.833 by roughly 1.1%. These improvements illustrate how Shazam leverages complementary multi-scale features from multiple foundation models to produce more discriminative and robust tile-level descriptors across varied tissue contexts. Although Shazam led performance on most benchmarks, its advantage narrowed in datasets where a single baseline model exhibited a pronounced task-specific strength. For instance, on UniToPatho, Virchow2 achieved a F1 score of 0.820, noticeably higher than the other individual models, and Shazam obtained 0.803, reflecting that the ensemble can inherit attenuated signals when several constituent models underperform. Even in such settings, Shazam remained consistently competitive across metrics, maintaining reliable performance despite variations in stain, scanner, and tissue preparation. This stability highlights Shazam’s capacity to generalize fine-grained morphological patterns at the tile level, where subtle artifacts, microenvironmental cues, and local histologic variability pose the greatest challenges for computational pathology models.

#### 4 Shazam improves pathology VQA

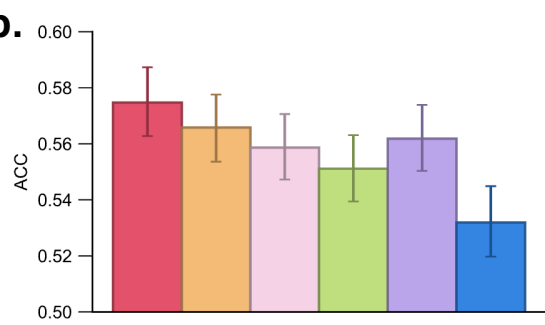
Visual Question Answering (VQA) aims to answer natural-language queries based on visual evidence and has emerged as a promising framework for assisting clinicians in retrieving task-specific diagnostic information from histopathology images. To examine Shazam’s capability in this setting, we used the PathVQA<sup>38</sup> dataset, which is among the largest resources for pathology VQA. The dataset contains 32,799 image–question–answer triplets, divided into a training set of 16,400 samples, a validation set of 9,840 samples, and a test set of 6,560 samples. Overall performance across the evaluated pathology foundation models is presented in Fig. 4b, with

detailed results provided in Supplementary Table 18.

**a.**



**b.**



**c.**

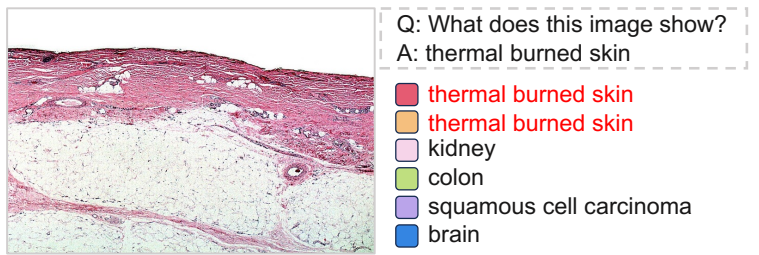


Figure 4: a, Quantitative comparison of tile-level performance across eleven classification benchmarks, measured by the F1 score for each foundation model. The first panel summarizes the average ranking of all models across tasks, where Shazam achieved the lowest (best) mean rank. The p-value shown in this panel corresponds to a one-sided Wilcoxon signed-rank test evaluating whether Shazam's rankings are significantly better than those of the strongest individual baseline. The remaining panels display the per-dataset distribution of F1 scores across repeated trials. b, Overall VQA accuracy for different pathology foundation models on the PathVQA test set. Error bars denote 95% confidence intervals obtained via 1000 times bootstrapping. Shazam achieves the highest accuracy among all evaluated models. c, A question and the answers generated by foundation models related to the query image.

Shazam achieved the highest accuracy of 0.575, exceeding the performance of the second-best model, UNI 2, by 1%. This result is notable because the foundation models underlying Shazam were trained exclusively

with image-based self-supervision and therefore received no explicit language or cross-modal guidance. Despite this limitation, the unified multi-model, multi-scale architecture of Shazam enabled strong performance on a task requiring alignment between visual patterns and linguistic queries. These findings indicate that Shazam’s integrative feature representation improves not only the discriminability of image-based features but also their transferability to cross-modal reasoning tasks. As a result, Shazam is able to extract visual cues from histopathology images that are relevant to the semantics of each question.

We further provide qualitative comparisons in Fig. 4c, where we illustrate a representative query image, question, and predicted answers across different foundation models. Shazam and UNI 2 consistently produced more reliable and clinically meaningful responses than the other evaluated models, supporting the quantitative advantages observed in the benchmark analysis.

## Discussion

In this work, we introduce Shazam, a unified pathology foundation model that consolidates the capabilities of multiple pretrained expert models without requiring access to their training data or performing any form of large-scale distillation pretraining. Previous efforts such as GPFM attempted to merge knowledge through offline distillation, yet their effectiveness is fundamentally limited by the diversity and scale of the available distillation corpus. Shazam adopts a fundamentally different integration strategy that operates in an online and task-specific manner, combining pretrained pathology foundation models through multi-level feature fusion and an adaptive expert-weighting mechanism. This design allows Shazam to continuously benefit from advances in pathology foundation models and to flexibly incorporate the most recent and most powerful models for any specific downstream task. With this ability, Shazam demonstrates consistently strong performance across four major categories of computational pathology, including spatial transcriptomics prediction, survival analysis, tile-level classification, and visual question answering in pathology. Across a total of 30 benchmark tasks, Shazam surpasses leading individual models such as UNI 2 and Virchow2 in the majority of evaluations.

The rapid development of pathology foundation models in recent years has markedly advanced the field, yet their pretraining pipelines continue to rely heavily on large, privately curated datasets whose composition varies substantially across institutions. These differences lead individual models to specialize in particular tissue types, staining styles or diagnostic tasks, which makes it difficult to ensure broad generalization across the diverse landscape of computational pathology. Moreover, because the underlying training data of these models are inaccessible, progress in foundation model development cannot accumulate at the data level, and each new model is effectively trained in isolation from its predecessors. Shazam addresses this structural limitation by allowing downstream tasks to selectively integrate the strengths of multiple pretrained models, without requiring access to any of their training corpora. Through this design, Shazam demonstrates robust generalization across heterogeneous tasks, suggesting that online integration of multiple foundation models represents a promising

direction for the next generation of computational pathology systems. This is particularly valuable in settings where different models capture distinct aspects of morphological or molecular variation, and where a single architecture is unlikely to dominate across all task domains.

Despite its strong empirical performance, Shazam has several limitations that warrant further investigation. Because Shazam requires all constituent foundation models to perform feature extraction during both training and inference, its computational cost grows approximately linearly with the number of integrated models. This requirement may limit its practicality in settings where low latency or constrained hardware resources are essential. Recent progress in developing lightweight pathology foundation models with substantially fewer parameters yet competitive performance provides a promising avenue for reducing this overhead<sup>39</sup>, and future versions of Shazam could incorporate such models to achieve a more favorable efficiency–performance balance. Another limitation lies in the breadth of external validation. Although Shazam demonstrates consistent gains across a wide range of internal benchmarks, the evaluation on independent datasets remains limited. Expanding external validation to additional cohorts and institutions will be important for fully establishing its robustness under real-world distributional variability. Continued exploration along these directions may further enhance the scalability, generalizability, and clinical readiness of Shazam.

## Online Methods

### Framework

#### 1 Shazam

Shazam is a multi-scale fusion framework designed to synthesize visual representations from diverse pathology foundation models. It consists of four key components: (1) multi-scale teacher feature extraction, (2) dimensional alignment, (3) adaptive mixture-of-experts (MoE) fusion, and (4) task-specific online distillation. Rather than relying on a single pretrained model, Shazam leverages complementary information distributed across different architectures and across multiple semantic scales.

**Multi-teacher and multi-scale representation extraction.** For each foundation model, we extract visual features at three characteristic depths—early, middle, and final layers—corresponding to low-, mid-, and high-level semantic representations. To ensure reproducibility across diverse architectures, we determine the extraction points mathematically. Let  $L$  denote the total number of transformer blocks in a given teacher model. We place non-invasive forward hooks at block indices defined by  $l_{\text{low}} = \lfloor 0.33 \times L \rfloor$ ,  $l_{\text{mid}} = \lfloor 0.66 \times L \rfloor$ , and  $l_{\text{high}} = L$ . During the training of Shazam, **all teacher models remain frozen** to serve as stable feature extrac-

tors. This strategy offers a consistent and lightweight mechanism for capturing multi-scale information across the five foundation models used in this study, namely UNI 2<sup>4</sup>, Virchow2<sup>16</sup>, H-optimus-1<sup>5</sup>, Prov-Gigapath<sup>9</sup>, and Phikon-v2<sup>17</sup>.

**Feature alignment and scale-wise fusion.** Because the teacher models operate in different embedding spaces, all extracted features are first mapped into a shared latent dimension using linear projection layers. At each semantic scale, Shazam then applies a Mixture-of-Experts (MoE)<sup>15</sup> module that learns to weight teacher-specific contributions. The MoE gating mechanism conditions on the concatenated teacher representations and produces an adaptive fusion, enabling the model to emphasize different visual experts depending on the input characteristics. The fused representations are refined through a small stack of self-attention blocks, which encourage information exchange across models. Higher-level fused features incorporate residual connections from preceding scales, allowing coarse structural cues from shallow layers to influence deeper semantic representations.

**Patch-to-slide aggregation for WSI tasks.** For whole-slide image (WSI) analysis, each teacher produces patch-level features at all three scales. These patch embeddings are aggregated into WSI-level representations using the Attention-Based Multiple Instance Learning (ABMIL) mechanism proposed by Ilse et al.<sup>40</sup>. Shazam employs scale-specific, independent ABMIL heads to aggregate features at each of the low, mid, and high scales, preserving hierarchical distinctiveness before the final fusion and prediction. Tile-level tasks directly use per-image features without patch aggregation.

**Distillation across scales and teachers.** To encourage the fused representation to preserve the strengths of individual foundation models, Shazam introduces a multi-level distillation objective. We apply  $L_2$ -normalization to both the student and teacher features before computing the distillation loss, which is essential for stable cosine distance calculation. This multi-scale approach encourages the student to maintain consistency with the teacher’s representations across different semantic hierarchies. For each scale  $s$ , the student feature  $z_s$  is aligned with each teacher’s feature vector  $t_s^{(i)}$  using a combination of normalized cosine distance and Huber loss:

$$\mathcal{L}_{\text{distill}}^{(s,i)} = \left( 1 - \frac{z_s \cdot t_s^{(i)}}{\|z_s\|_2 \|t_s^{(i)}\|_2} \right) + \text{Huber}(z_s, t_s^{(i)}),$$

The overall distillation loss averages across all scales and all  $N = 5$  teachers:

$$\mathcal{L}_{\text{distill}} = \frac{1}{3N} \sum_{s \in \{\text{low, mid, high}\}} \sum_{i=1}^N \mathcal{L}_{\text{distill}}^{(s,i)}.$$

**Training objective.** Shazam is trained jointly with task-specific supervision signals such as cross-entropy for classification or negative log-likelihood for survival analysis. The final objective combines the task-level loss ( $\mathcal{L}_{\text{task}}$ ) and the multi-scale distillation loss ( $\mathcal{L}_{\text{distill}}$ ):

$$\mathcal{L} = \mathcal{L}_{\text{task}} + \lambda_{\text{distill}} \mathcal{L}_{\text{distill}},$$

where  $\lambda_{\text{distill}} = 0.01$  controls the strength of the distillation constraint. This formulation allows Shazam to adapt to individual downstream tasks while maintaining consistency with the representational structures encoded by the frozen teacher models.

For optimization, we use the AdamW optimizer with a weight decay of  $1 \times 10^{-4}$  and employ a cosine learning rate schedule. The model is trained for 50 epochs with a batch size of 128.

Overall, Shazam provides a unified representation-learning module capable of harmonizing information from multiple pathology foundation models and across several semantic scales, enabling improved robustness and transferability across diverse computational pathology applications.

## 2 Comparisons & Baselines

To ensure a fair and controlled evaluation, all baseline pathology foundation models were assessed using the same downstream pipelines as Shazam. Each baseline was used strictly as a frozen feature extractor according to its official implementation, and all downstream components were kept identical across methods. This includes the task-specific prediction heads as well as the ABMIL module for whole-slide analysis. Patch embeddings were consistently taken from the final transformer block of each baseline model. By standardizing the feature extraction procedure, the aggregation architecture, and the optimization settings, the comparisons isolate the representational differences among models and ensure that performance variation reflects the intrinsic quality of the learned features.

## Tasks and datasets

## 3 Spatial Transcriptomic Experiments

Spatial transcriptomics measures gene expression while preserving the anatomical location of each measurement within intact tissue sections <sup>18</sup>. By linking RNA abundance directly to histological context, these technologies enable spatially resolved characterization of cell states, signaling programs, and tumor–microenvironment interactions that cannot be inferred from morphology or bulk profiling alone <sup>18,41</sup>. This integration of molecular

and histologic information provides a powerful framework for understanding tissue organization and disease progression.

To define clinically meaningful prediction targets, we curated cohort-specific gene lists guided by FDA-recognized biomarkers in OncoKB<sup>42</sup>. Cohort-level preprocessing was then applied to reduce sparsity and ensure adequate expression signal. Slides were excluded if at least half of the selected genes had zero expression, and genes were excluded if they were zero in at least half of the slides within the same cohort. The resulting filtered datasets were used for all downstream analyses. Cohort-specific gene lists are summarized in Supplementary Table 1.

We conducted experiments using the publicly available HEST 1k dataset<sup>24</sup>, which provides paired spatial transcriptomic profiles and matched H&E-stained whole-slide images across diverse organs. From this dataset, we selected eight organ-specific cohorts with sufficient paired samples: breast, prostate, skin, bowel, liver, kidney, brain, and bladder. To prevent patient-level data leakage, we followed a patient-stratified protocol: samples without patient identifiers were assigned exclusively to the training pool, and samples with identifiers were split at the patient level so that all spots and patches from each patient occurred within a single fold<sup>24</sup>.

Model inputs were constructed by extracting H&E patches of  $112 \times 112 \mu\text{m}$ , corresponding to  $224 \times 224$  pixels at  $20\times$  magnification, paired with their matched gene expression vectors. Models were trained using patient-level  $k$ -fold cross-validation with  $k = \min(5, N_{\text{patients}})$ . Prior to training, gene expression was cohort-wise log-normalized to stabilize variance. The student regressor consisted of a deep MLP; expert features were concatenated and fused using stacked cross-attention layers, followed by an MLP with GELU activations and dropout, and a final linear output layer predicting all target genes. Optimization used AdamW with a learning rate of  $1 \times 10^{-3}$  for 30 epochs and a validation-driven scheduler. The loss combined ridge regression (mean squared error with  $L_2$  regularization) with a multi-level distillation term, forming  $\mathcal{L} = \mathcal{L}_{\text{ridge}} + \lambda_{\text{distill}} \mathcal{L}_{\text{distill}}$ , where  $\lambda_{\text{distill}} = 0.01$ .

## 4 Patch-level Classification

For each foundation model, we load its official pretrained weights and extract tile-level representations following the recommended preprocessing settings. This ensures that all models are evaluated under a consistent and standardized protocol.

Based on these extracted features, we train a multilayer perceptron (MLP) classifier composed of two fully connected layers with LayerNorm and GELU activation, followed by a final linear prediction layer. Optimization is performed using Adam with a learning rate of  $1 \times 10^{-3}$ , a batch size of 64, and a maximum of 100 epochs with early stopping (patience = 30). This procedure is used to assess the representational quality and transferability of each foundation model when used in isolation.

For our method, Shazam, tile-level features are first extracted from all five foundation models at three semantic scales. These multi-scale features are subsequently fused through the Shazam framework: each scale is processed by a Mixture-of-Experts module to adaptively combine information across models, followed by layers of self-attention to refine cross-model interactions. The resulting fused representation is then passed to the same MLP classifier used for the baselines. During training, we additionally apply a multi-level distillation objective that aligns the fused Shazam feature at each scale with its corresponding teacher-specific representation, encouraging the fused embedding to inherit complementary signals from all foundation models.

The overall training objective is defined as:

$$\mathcal{L} = \mathcal{L}_{\text{CE}} + \lambda_{\text{distill}} \mathcal{L}_{\text{distill}},$$

where  $\lambda_{\text{distill}} = 0.01$ . The distillation term is composed of a cosine-similarity loss and a Huber loss applied at each semantic scale. To properly handle class imbalance, we report Balanced Accuracy, Weighted F1, and AUC as the evaluation metrics.

### **HunCRC for CRC Tissue Classification (9 classes).**

This dataset comprises 101,398 H&E-stained image patches, also referred to as regions of interest (ROIs), each measuring  $512 \times 512$  pixels at a resolution of 0.48 microns per pixel (mpp). These ROIs were extracted from 200 formalin-fixed paraffin-embedded (FFPE) whole-slide images (WSIs) of colorectal biopsies<sup>28</sup>. Designed to support the training of machine learning models for colorectal tissue classification, the dataset includes annotations for nine classes: Adenocarcinoma (4,315 ROIs), High-Grade Dysplasia (2,281 ROIs), Low-Grade Dysplasia (55,787 ROIs), Inflammation (763 ROIs), Tumor Necrosis (365 ROIs), Suspicious for Invasion (570 ROIs), Resection Edge (534 ROIs), Technical Artifacts (3,470 ROIs), and Normal Tissue (31,323 ROIs). For training and evaluation, the dataset follows the official split, with 76,753 ROIs used for training, 11,327 ROIs for validation, and 11,328 ROIs for testing. The experimental results for this dataset are reported in Supplementary Table 4.

### **UniToPatho for CRC Polyp Classification (6 classes).**

This dataset comprises 9,536 H&E-stained image patches (ROIs) extracted from 292 whole-slide images (WSIs)<sup>29</sup>. Its primary purpose is to facilitate the training of deep neural networks for colorectal polyp classification and adenoma grading. The dataset includes annotations for six classes: Normal Tissue (950 ROIs), Hyperplastic Polyp (545 ROIs), Tubular Adenoma with High-Grade Dysplasia (454 ROIs), Tubular Adenoma with Low-Grade Dysplasia (3,618 ROIs), Tubulo-Villous Adenoma with High-Grade Dysplasia (916 ROIs), and Tubulo-Villous Adenoma with Low-Grade Dysplasia (2,186 ROIs). For training and evaluation, the dataset follows the official split, with 6,270 ROIs used for training, 1,199 ROIs for validation, and 1,200 ROIs for testing. The experimental results for this dataset are reported in Supplementary Table 5.

### **PCAM for Metastatic Tissue Classification (2 classes).**

PCAM consists of 327,680 color images with a resolution of  $96 \times 96$  pixels, extracted from the CAMELYON16 dataset<sup>3043</sup>. Each image is annotated with a binary label indicating the presence of metastatic tissue. For training and evaluation, we adopt the official train-validation-test split of 262,144, 32,768, and 32,768 ROIs, respectively, and resize all images to  $224 \times 224$  pixels. The experimental results for this dataset are reported in Supplementary Table 6.

### **ESCA for Esophageal Carcinoma Subtyping (11 classes).**

ESCA contains 367,229 patches, each with a resolution of  $256 \times 256$  pixels, sourced from various institutions: University Hospital Cologne (UKK), Landesklinikum Wiener Neustadt (WNS), TCGA, and University Hospital Berlin Charité (CHA)<sup>44</sup>. These patches were annotated into 11 classes, including adventitia, lamina propria mucosae, muscularis mucosae, muscularis propria, regression tissue, mucosa gastric, mucosa esophagus, submucosa, submucosal glands, tumor, and ulceration. For training and evaluation, we use the CHA dataset (178,187 ROIs) as the training set and combine UKK, WNS, and TCGA (189,142 ROIs) for testing. All images were resized to  $224 \times 224$  pixels. The experimental results for this dataset are reported in Supplementary Table 7.

### **PanCancer-TIL for TIL classification (2 classes).**

PanCancer-TIL consists of 304,097 images with a resolution of  $100 \times 100$  pixels, labeled as TIL-positive (54,910 ROIs) and TIL-negative (249,187 ROIs)<sup>32</sup>. The official train-validation-test split of 209,221, 38,601, and 56,275 ROIs is adopted, and all images are resized to  $256 \times 256$  pixels. The experimental results for this dataset are reported in Supplementary Table 8.

### **CRC-100K for Colorectal Cancer (CRC) Tissue Classification (9 classes).**

The CRC-100K dataset is composed of the NCT-CRC-HE-100K and CRC-VAL-HE-7K cohorts<sup>45</sup>. NCT-CRC-HE-100K contains 100,000 non-overlapping  $224 \times 224$  H&E patches sourced from 86 colorectal cancer whole-slide images obtained from the NCT biobank and the UMM pathology archive. The CRC-VAL-HE-7K subset includes 7,180  $224 \times 224$  patches collected from 50 patients diagnosed with colorectal adenocarcinoma. The dataset covers nine histological tissue categories: adipose (ADI, 11,745 ROIs), background (BACK, 11,413), debris (DEB, 11,851), lymphocytes (LYM, 12,191), mucus (MUC, 9,931), smooth muscle (MUS, 14,128), normal colon mucosa (NORM, 9,504), cancer-associated stroma (STR, 10,867), and colorectal adenocarcinoma epithelium (TUM, 15,550). We follow the official train–test split of 100,000 and 7,180 patches, respectively. The experimental results for this dataset are reported in Supplementary Table 9.

### **CCRCC-TCGA-HEL for CCRCC Tissue Classification (4 classes).**

This dataset consists of 52,713 regions of interest (ROIs), each with a resolution of  $300 \times 300$  pixels, from TCGA-KIRC and Helsinki<sup>33</sup>. The dataset includes six categories: renal cancer (cancer, 13,057 ROIs), normal renal tissue (normal, 8,652 ROIs), stromal tissue (stroma, 5,460 ROIs), red blood cells (blood, 996 ROIs), empty background (empty, 16,026 ROIs), and other textures (other, 8,522 ROIs). For training and evaluation, we focus on four specific categories: cancer, stroma, normal, and blood, excluding the "empty" and "other" categories. The samples are shuffled and split using a 22,530:5,635 ratio for train/test. The experimental results for this dataset are reported in Supplementary Table 10.

### **BACH for Breast Cancer Tissue Classification (4 classes).**

The BACH dataset consists of 400 images ( $2048 \times 1536$  pixels) labeled into four classes: Normal (100 ROIs), Benign (100 ROIs), In situ carcinoma (100 ROIs), and Invasive carcinoma (100 ROIs)<sup>34</sup>. For training and evaluation, all ROIs are resized to  $224 \times 224$  pixels, and a label-stratified train-test split of 320:80 ROIs is used. The experimental results for this dataset are reported in Supplementary Table 11.

### **CRC-MSI for MSI Screening (2 classes).**

The CRC-MSI dataset includes 51,918 histology images with a resolution of  $512 \times 512$  pixels, obtained from the TCGA database<sup>35</sup>. The images are annotated with MSI status, where patients are classified as MSI-H (high MSI) or NonMSIH (either MSI-L or MSS). For training and evaluation, we use the official 19,557:32,361 train-test split. The experimental results for this dataset are reported in Supplementary Table 12.

### **PanCancer-TCGA for Tissue Classification (32 classes).**

The PanCancer-TCGA dataset contains 271,170 images with dimensions  $256 \times 256$  pixels, extracted from 8,736 TCGA WSIs across 32 different cancer types<sup>36</sup>. The images are annotated with 32 classes, including Head and Neck Squamous Cell Carcinoma (11,790 ROIs), Bladder Urothelial Carcinoma (9,990 ROIs), Lung Squamous Cell Carcinoma (16,560 ROIs), Glioblastoma Multiforme (23,740 ROIs), among others. For training and evaluation, we use a 21,736:54,342 train/test split. The experimental results for this dataset are reported in Supplementary Table 13.

### **Chaoyang for Colon Tissue Classification (4 classes).**

The Chaoyang dataset includes colon tissue patches from Chaoyang hospital, comprising 1,816 normal ROIs, 1,163 serrated ROIs, 2,244 adenocarcinoma ROIs, and 937 adenoma ROIs<sup>37</sup>. For training and evaluation, all patches are resized to  $224 \times 224$  pixels, and the official train-test split (4,021:2,139 ROIs) is used. The experimental results for this dataset are reported in Supplementary Table 14.

## 5 Survival Analysis

Survival analysis has long been a standard approach for modeling time-to-event data in oncology, focusing on outcomes such as disease progression or overall survival. When applied to whole-slide images (WSIs), it provides new opportunities to explore tissue-level patterns and predict patient outcomes. By integrating survival analysis with WSIs, researchers can examine correlations between specific morphological characteristics and clinical prognosis.

To preprocess whole-slide images (WSIs), we adopt the CLAM pipeline<sup>46</sup> to perform tissue foreground segmentation and extract valid regions. From these foreground masks, we crop non-overlapping patches at  $20\times$  magnification and resize each patch to  $224\times 224$  pixels for feature extraction. Slides containing too few valid patches after segmentation are excluded. The resulting patch set for each WSI is then passed to pathology foundation models to obtain patch-level embeddings for subsequent MIL-based slide analysis.

In this study, we adopt the Attention-Based Multiple Instance Learning (ABMIL) framework<sup>40</sup> for survival analysis, employing the Negative Log-Likelihood (NLL) loss. we introduce a distillation loss term for model compression. Specifically, we employ Shazam student model, distilled from a larger teacher model, using a weighted distillation loss with  $\lambda = 0.01$  to align the student’s predictions with the teacher’s. Optimization is performed using AdamW with a learning rate of  $2 \times 10^{-4}$  and weight decay of  $1 \times 10^{-3}$ .The dataset partitioning strategy follows that described in the GPFM study<sup>47</sup>. To assess the impact of different pathology foundation models on survival prediction, we perform 5-fold cross-validation and use the C-index as the evaluation metric.

Experiments are conducted on 10 TCGA datasets: TCGA-BRCA, TCGA-BLCA, TCGA-KIRC, TCGA-LUAD, TCGA-STAD, TCGA-LUSC, TCGA-COADREAD, TCGA-GBMLGG, TCGA-SKCM, and TCGA-CESC. The results are reported in Supplementary Data Table 4- 7.

### Breast Cancer Survival Prediction.

We leverage the TCGA-BRCA dataset<sup>48</sup> for breast cancer survival prediction, which consists of 1,023 cases (1,089 WSIs). Following the GPFM partitioning strategy, we maintain uniform censorship between the training and testing sets and apply stratified binning of survival times into four equally sized bins. For each fold of the 5-fold cross-validation, we perform an 8:2 label-stratified split, resulting in 821 training cases and 202 testing cases. The mean C-index and standard deviation across the folds are presented in Extended Data Table A16.

### **Bladder Cancer Survival Prediction.**

For bladder cancer survival prediction, we use the TCGA-BLCA dataset<sup>48</sup>, containing 376 cases (446 WSIs). Using the same stratified binning and partitioning strategy as BRCA, each fold allocates 305 cases to training and 71 cases to testing. The results are shown in the BLCA column of Extended Data Table A16.

### **Kidney Renal Clear Cell Carcinoma Survival Prediction.**

The TCGA-KIRC dataset<sup>48</sup> comprises 498 cases (504 WSIs). Following the same partitioning strategy, each fold assigns 401 cases to training and 97 cases to testing. Results are reported in the KIRC column of Extended Data Table A16.

### **Stomach Adenocarcinoma Survival Prediction.**

The TCGA-STAD dataset<sup>48</sup> contains 363 cases (389 WSIs). In each fold, 293 cases are allocated to training and 70 to testing using the same stratified splitting procedure. Results are shown in the STAD column of Extended Data Table A17.

### **Cervical Squamous Cell Carcinoma and Endocervical Adenocarcinoma Survival Prediction.**

The TCGA-CESC<sup>48</sup> dataset includes 250 cases (260 WSIs). Using the same strategy, we assign 203 cases to training and 47 cases to testing per fold. Results are presented in the CESC column of Extended Data Table A17.

### **Lung Adenocarcinoma Survival Prediction.**

For TCGA-LUAD<sup>48</sup>, we use 455 cases (518 WSIs), splitting each fold into 366 training cases and 89 testing cases. Results for both datasets are shown in Extended Data Table A18.

## **Lung Squamous Cell Carcinoma Survival Prediction.**

The TCGA-LUSC dataset<sup>48</sup> comprises 452 cases (484 WSIs). Using the same stratified splitting approach, 365 cases are assigned to training and 87 to testing in each fold. Results are reported in Extended Data Table A18.

## **Colon & Rectum Adenocarcinoma Survival Prediction.**

We combine TCGA-COAD<sup>48</sup> (426 cases, 434 WSIs) and TCGA-READ (153 cases, 154 WSIs) into a single dataset of 579 cases (588 WSIs). Each fold assigns 464 cases to training and 115 to testing. Results are shown in Extended Data Table A19.

## **Glioma Survival Prediction.**

We merge TCGA-GBM (370 cases, 823 WSIs) and TCGA-LGG<sup>48</sup> (460 cases, 778 WSIs) into a combined glioma dataset of 830 cases (1,601 WSIs). Per fold, 667 cases are used for training and 163 for testing. Results are in Extended Data Table A19.

## **Skin Cutaneous Melanoma Survival Prediction.**

The TCGA-SKCM dataset<sup>48</sup> contains 415 cases (456 WSIs). Each fold uses 337 cases for training and 78 for testing. Results are shown in Extended Data Table A19.

## **6 Pathology VQA**

We evaluate our pathology foundation models on the PathVQA benchmark<sup>38</sup>, a standard dataset for assessing visual question answering (VQA) capabilities in pathology. PathVQA requires models to jointly interpret visual content and natural-language questions, providing a comprehensive assessment of multimodal medical reasoning. We adopt the Multi-modal Unified Medical Captioning (MUMC) framework<sup>49</sup>, which demonstrates strong performance on PathVQA by tightly integrating textual and visual representations.

The VQA model architecture consists of four main components: the image encoder, text encoder, multimodal encoder, and answering decoder. The only architectural modification we introduce lies in the image

encoding stage. Instead of the single ViT encoder used in the original MUMC design, we integrate Shazam as a multi-level visual expert. Shazam provides hierarchical low-, mid-, and high-level pathology representations, which are further combined with features extracted from four additional pathology foundation models. These multi-model and multi-level visual features are fused through a Mixture-of-Experts mechanism followed by a sequence of cross-attention layers. The resulting fused embedding is projected into a 768-dimensional space to match the input requirements of the subsequent multimodal Transformer.

All remaining components of the architecture strictly follow the original MUMC configuration. The text encoder processes each question using the first six layers of a pre-trained BERT model, functioning as a pure language encoder. The multimodal encoder corresponds to the final six layers of the same BERT model, each incorporating cross-attention to fuse the projected visual embeddings with the intermediate textual representations. This two-stage design allows the model to first capture the linguistic structure of the question before grounding it in visual evidence drawn from Shazam and the other pathology foundation models. The answering decoder, implemented as a 6-layer Transformer language model, autoregressively generates answer tokens conditioned on the multimodal representations.

During training, all Shazam parameters remain frozen to preserve its domain-specific visual representation. The model is fine-tuned for 40 epochs using AdamW, with the learning rate decayed from  $2 \times 10^{-5}$  to  $1 \times 10^{-8}$  to ensure stable optimization. The training objective includes a standard cross-entropy loss for answer generation, combined with a hierarchical distillation loss that supervises the fused MoE representations using multi-level teacher features from the five foundation models. This distillation strategy encourages the student model to align its fused representation with the teacher experts at the low-, mid-, and high-level semantic hierarchies, further improving cross-modal alignment and VQA performance.

The experimental results are summarized in Supplementary Table 18. Integrating Shazam as a multi-level visual expert leads to a substantial improvement in accuracy, demonstrating the effectiveness of hierarchical feature integration for supporting fine-grained multimodal reasoning in pathology.

## Computing hardware and software

All experiments were conducted in the Python environment (Python 3.10.0). Model training and inference were performed using PyTorch (version 2.8.0, compiled with CUDA 12.8), together with TorchVision 0.23.0. Downstream machine learning experiments used Scikit-learn 1.7.2 and NumPy 2.2.6. Whole-slide image (WSI) processing relied on the OpenSlide-Python interface (version 1.4.2) as well as the CLAM<sup>46</sup> codebase. For WSI processing, we relied on openslide-python (version 1.2.0) and the CLAM<sup>46</sup> codebase. Pathology VQA evaluation was conducted using the MUMC<sup>49</sup> codebase. All computations were executed on a workstation equipped with 8 × NVIDIA GeForce RTX 4090 GPUs.

## Data availability

The HEST-1k dataset used in this study is publicly available at Hugging Face (<https://huggingface.co/datasets/MahmoodLab/hest>). Processed data and model outputs generated during this study are available from the corresponding author upon reasonable request.

The Survival Analysis tasks are based on clinical and genomic data that can be accessed through the GDC Data Portal (<https://portal.gdc.cancer.gov/>).

The PathVQA dataset used for visual question answering experiments is available at Github (<https://github.com/UCSD-AI4H/PathVQA>).

All tile-level classification tasks in this study are conducted on publicly available histopathology datasets, including:

- HunCRC (<https://www.cancerimagingarchive.net/collection/hungarian-colorectal>)
- UniToPatho (<https://github.com/EIDOSLAB/UNITOPATHO>)
- PCAM (<https://github.com/basveeling/pcam>)
- ESCA (<https://zenodo.org/records/7548828>)
- PanCancer-TIL (<https://zenodo.org/records/6604094>)
- CRC-100K (<https://zenodo.org/records/1214456>)
- CCRCC-TCGA-HEL (<https://zenodo.org/records/7898308>)
- BACH (<https://zenodo.org/records/3632035>)
- CRC-MSI (<https://zenodo.org/records/3832231>)
- PanCancer-TCGA (<https://zenodo.org/records/5889558>)
- Chaoyang dataset (<https://github.com/bupt-ai-cz/HSA-NRL>)

## Code availability

The code of the Shazam have been made available on GitHub <https://github.com/Tuner12/Shazam>

## **Author contributions**

Conceptualization: W.L., Y.T., A.L., H.C., X.Z., and S.Z. Methodology: W.L., Y.T., A.L., X.Z., and S.Z. Investigation: W.L., Y.T., A.L., H.C., H.T., R.L., F.Y. Visualization: W.L., Y.T., A.L. Funding acquisition: X.Z., S.Z. Supervision: X.Z., S.Z. Writing: W.L., Y.T., A.L.

## **Acknowledgements**

## Supplementary Files

Supplementary Table 1: **Cancer-specific gene lists for HEST-1k.** Gene prioritization was informed by the FDA-recognized content in OncoKB <sup>42</sup>.

Cancer	Gene list
breast	ALK;APC;AR;ARAF;ARID1A;ATM;BRAF;BRCA1;BRCA2;CCND1;CD274;CDH1;CDKN1B;CDKN2A;CHEK2;CREBBP;EGFR;ERBB2;ERBB3;ESR1;FBXW7;FGFR1;FGFR2;FGFR3;FLT3;FOXA1;GATA3;GNAS;IDH1;IDH2;JAK1;JAK2;KDR;KEAP1;KIT;KRAS;MAP2K1;MAP2K2;MAPK1;MDM2;MET;MLH1;MSH2;MSH6;MTOR;MUTYH;MYC;NF1;NOTCH1;NTRK1;NTRK2;NTRK3;PALB2;PBRM1;PDCD1LG2;PIK3CA;PIK3R1;PMS2;POLD1;POLE;PTEN;RAD51C;RAD51D;RB1;RET;ROS1;SMAD4;SMARCA4;SMARCB1;STK11;TP53;TSC1;TSC2;VHL
bowel	ALK;APC;ARID1A;ATM;BRAF;BRCA1;BRCA2;CCND1;CD274;CDKN2A;CHEK2;CTNNB1;EGFR;ERBB2;ERBB3;FBXW7;FGFR1;FGFR2;FGFR3;FLT3;GNAS;IDH1;IDH2;JAK1;JAK2;KDR;KIT;KRAS;MAP2K1;MAP2K2;MAPK1;MET;MLH1;MSH2;MSH6;MTOR;MYC;NF1;NTRK1;NTRK2;NTRK3;PALB2;PDCD1LG2;PIK3CA;PIK3R1;PMS2;POLD1;POLE;PTEN;RAD51C;RAD51D;RB1;RET;ROS1;SMAD4;SMARCA4;SMARCB1;TP53;TSC1;TSC2;VHL
kidney	CDKN2A;FGFR2;MED12;PIK3CA;TERT;ALK;CDKN2B;FGFR1;FLCN;KIT;MET;NTRK3;PTEN;SMARCB1;TP53;ARAF;DAXX;FGFR3;H3F3A;KRAS;MTOR;PBRM1;RBI;TSC2;ATM;EGFR;FH;HRAS;MAP2K1;NF1;PDGFRA;SETD2;VHL;BRAF;ERBB2;GNAQ;IDH1;MAP2K2;NTRK1;POLQ;SMAD4;WT1;CDK4;ERBB3;GNAS;IDH2;MAPK1;NTRK2;PPM1D;SMARCA4;DICER1;EZH2;GNA11;JAK2;MDM2;RET;SMARCB1;TSC1;CTNNB1;FGFR4;HNF1A;KDR;MYC;ROS1;SOX9
brain	ABCC2;ABCC4;ABCG2;ABL1;ABRAXAS1;ALK;APC;AR;ARID1A;ATM;ATR;AXIN1;B2M;BAP1;BARD1;BCL2L1;BCR;BLM;BRAF;BRCA1;BRCA2;BRIP1;BTK;CARD11;CCND1;CCND2;CCND3;CD274;CDK12;CDK4;CDK6;CDKN2A;CDKN2B;CEBPA;CHEK1;CHEK2;CIC;CREBBP;CRKL;CSF1R;CTNNB1;CUL3;DAXX;DDR2;DIS3;DNMT3A;EGFR;EP300;EPCAM;ERBB2;ERBB3;ERCC2;ERCC3;ERCC4;ERCC5;ESR1;EZH2;FAM175A;FANCA;FANCC;FANCD2;FANCE;FANCF;FANCG;FAS;FBXW7;FGFR1;FGFR2;FGFR3;FGFR4;FH;FLCN;FLT3;FOXL2;GATA2;GATA3;GNA11;GNAQ;GNAS;H3F3A;HNF1A;HRAS;IDH1;IDH2;IFITM1;IFNGR1;IGF1R;IL7R;JAK1;JAK2;JAK3;KDR;KEAP1;KIT;KRAS;MAP2K1;MAP2K2;MAPK1;MECOM;MED12;MET;MDM2;MDM4;MLH1;MSH2;MSH6;MTOR;MUTYH;MYC;NF1;NF2;NOTCH1;NOTCH2;NPM1;NRAS;NRG1;NTRK1;NTRK2;NTRK3;PALB2;PDCD1LG2;PDGFRA;PIK3CA;PIK3R1;PMS2;POLE;POLD1;PPP2R1A;PPARG;PRKAR1A;PTCH1;PTEN;RAD51C;RAD51D;RAF1;RB1;RET;RHOA;ROS1;RUNX1;SETD2;SMAD4;SMARCA4;SMARCB1;SOCS1;SOX9;SPOP;SRC;STK11;SUFU;TERT;TGFBR2;TP53;TSC1;TSC2;VHL;WT1
skin	CDK6;FANCE;JAK3;NRG1;RUNX1;ACVR1;CDK8;FANCF;JUN;PDGFRA;SMARCB1;AKT1;CDKN2A;FANCG;KDM6A;PIK3CA;SMO;ALK;CIC;FANCL;KEAP1;PIK3R1;SMARCA4;APC;CREBBP;FBXW7;KIT;PMS2;SMARCB1;AR;CSF1R;FLCN;KRAS;POLE;SMARCB1;ARAF;CTNNB1;FLT3;MAP2K1;POLD1;SRC;ARID1A;DAXX;GNA11;MAP2K2;PPP2R1A;STK11;ATM;DDR2;GNAQ;MAPK1;PTCH1;SUFU;BRAF;DNMT3A;GNAS;MECOM;PTEN;TERT;BRCA1;EGFR;H3F3A;MED12;PTPN11;TGFBR2;BRCA2;EP300;HRAS;MET;RAF1;TP53;CCND1;ERBB2;IDH1;MDM2;RB1;TSC1;CCND2;ERBB3;IDH2;MDM4;RET;TSC2;CCND3;ERCC2;IGF1R;MLH1;RHOA;VHL;CD274;EZH2;JAK1;MSH2;ROS1;WT1;CDK12;FGFR1;JAK2;MSH6;SETD2;AXIN1;B2M;BAP1;BARD1;BCL2L1;BCR;BLM;BRIP1;BTK;CARD11;CEBPA;CHEK1;CHEK2;CIC;CRKL;CUL3;DIS3;EPCAM;ERCC3;ERCC4;ERCC5;ESR1;FAM175A;FANCA;FANCC;FANCD2;FAS;FGFR2;FGFR3;FGFR4;FH;FOXL2;GATA2;GATA3;HNF1A;IFITM1;IFNGR1;IL7R;KDR;MECOM;MDM2;MDM4;MTOR;MUTYH;MYC;NF1;NF2;NOTCH1;NOTCH2;NPM1;NRAS;NTRK1;NTRK2;NTRK3;PALB2;PDCD1LG2;PIK3CA;PIK3R1;PMS2;POLE;POLD1;PPARG;PRKAR1A;PTCH1;PTEN;RAD51C;RAD51D;RAF1;RB1;RET;RHOA;ROS1;SETD2;SMAD4;SMARCA4;SOCS1;SOX9;SPOP;STK11;SUFU;TERT;TGFBR2;TP53;TSC1;TSC2;VHL;WT1
liver	ALK;ARID1A;ATM;BRAF;BRCA1;BRCA2;CCND1;CD274;CDKN2A;CTNNB1;EGFR;ERBB2;ERBB3;FBXW7;FGFR1;FGFR2;FGFR3;IDH1;IDH2;JAK1;JAK2;KDR;KIT;KRAS;MAP2K1;MAP2K2;MAPK1;MET;MLH1;MSH2;MSH6;MTOR;MYC;NF1;NTRK1;NTRK2;NTRK3;PALB2;PDCD1LG2;PIK3CA;PIK3R1;PMS2;POLD1;POLE;PTEN;RAD51C;RAD51D;RB1;RET;ROS1;SMAD4;SMARCA4;SMARCB1;STK11;TP53;TSC1;TSC2;VHL
prostate	ALK;APC;AR;ATM;BRAF;BRCA1;BRCA2;CCND1;CD274;CDK12;CDKN2A;CHEK2;EGFR;ERBB2;ERBB3;FBXW7;FGFR1;FGFR2;FGFR3;FLT3;FOXA1;IDH1;IDH2;JAK1;JAK2;KDR;KIT;KRAS;MAP2K1;MAP2K2;MAPK1;MDM2;MLH1;MSH2;MSH6;MTOR;MYC;NF1;NTRK1;NTRK2;NTRK3;PALB2;PDCD1LG2;PIK3CA;PIK3R1;PMS2;POLD1;POLE;PTEN;RAD51C;RAD51D;RB1;RET;ROS1;SMAD4;SMARCA4;SMARCB1;TP53;TSC1;TSC2;VHL
bladder	ALK;APC;ARID1A;ATM;BRAF;BRCA1;BRCA2;CCND1;CD274;CDKN2A;CHEK2;CREBBP;EGFR;ERBB2;ERBB3;ERCC2;FBXW7;FGFR1;FGFR2;FGFR3;FLT3;GNAS;IDH1;IDH2;JAK1;JAK2;KDR;KIT;KRAS;MAP2K1;MAP2K2;MAPK1;MET;MLH1;MSH2;MSH6;MTOR;MYC;NF1;NTRK1;NTRK2;NTRK3;PALB2;PDCD1LG2;PIK3CA;PIK3R1;PMS2;POLD1;POLE;PTEN;RAD51C;RAD51D;RB1;RET;ROS1;SMAD4;SMARCA4;SMARCB1;STK11;TP53;TSC1;TSC2;VHL;ERCC3;ERCC4;ERCC5;TERT;TSC1;TSC2

Supplementary Table 2: **ST prediction performance of different foundation models on Hest-1k dataset (Part 1/2).** The 95% CI is included in parentheses. Best model is **bolded**, second-best is underlined.

Model	Organ	PCC	Num	Test patient num
UNI 2	breast	<u>0.162 (0.091–0.233)</u>	125	36
Virchow2	breast	<u>0.137 (0.066–0.207)</u>	125	36
H-optimus-1	breast	0.147 (0.099–0.196)	125	36
Prov-Gigapath	breast	0.123 (0.057–0.189)	125	36
Phikon-v2	breast	0.139 (0.058–0.219)	125	36
Shazam	breast	<b>0.178 (0.078–0.278)</b>	125	36
UNI 2	prostate	0.143 (-0.073–0.359)	60	2
Virchow2	prostate	0.143 (-0.170–0.456)	60	2
Prov-Gigapath	prostate	0.138 (-0.049–0.324)	60	2
Phikon-v2	prostate	0.145 (-0.278–0.569)	60	2
H-optimus-1	prostate	<u>0.161 (-0.217–0.539)</u>	60	2
Shazam	prostate	<b>0.191 (-0.170–0.552)</b>	60	2
UNI 2	skin	<u>0.104 (0.075–0.133)</u>	27	7
Virchow2	skin	<u>0.101 (0.071–0.130)</u>	27	7
Prov-Gigapath	skin	0.091 (0.062–0.121)	27	7
Phikon-v2	skin	0.098 (0.062–0.135)	27	7
H-optimus-1	skin	0.098 (0.068–0.129)	27	7
Shazam	skin	<b>0.121 (0.087–0.154)</b>	27	7
UNI 2	bowel	0.213 (0.144–0.281)	64	6
Virchow2	bowel	0.203 (0.147–0.260)	64	6
H-optimus-1	bowel	0.203 (0.148–0.259)	64	6
Prov-Gigapath	bowel	0.209 (0.150–0.268)	64	6
Phikon-v2	bowel	<u>0.219 (0.162–0.276)</u>	64	6
Shazam	bowel	<b>0.239 (0.153–0.326)</b>	64	6

Supplementary Table 3: **ST prediction performance of different foundation models on Hest-1k dataset (Part 2/2).** The 95% CI is included in parentheses. Best model is **bolded**, second-best is underlined.

Model	Organ	PCC	Num	Test patient num
UNI 2	liver	0.051 (0.040–0.062)	13	2
Virchow2	liver	<u>0.073</u> (-0.138–0.283)	13	2
Prov-Gigapath	liver	<u>0.060</u> (0.009–0.110)	13	2
Phikon-v2	liver	0.061 (0.010–0.111)	13	2
H-optimus-1	liver	0.059 (-0.049–0.167)	13	2
Shazam	liver	<b>0.149</b> <b>(-0.043–0.341)</b>	13	2
UNI 2	kidney	0.213 (0.163–0.262)	25	24
Virchow2	kidney	0.203 (0.158–0.249)	25	24
H-optimus-1	kidney	<u>0.203</u> (0.169–0.237)	25	24
Prov-Gigapath	kidney	0.209 (0.161–0.257)	25	24
Phikon-v2	kidney	<u>0.219</u> (0.192–0.247)	25	24
Shazam	kidney	<b>0.239</b> <b>(0.189–0.288)</b>	25	24
UNI 2	brain	0.091 (0.064–0.118)	24	11
Virchow2	brain	0.089 (0.072–0.105)	24	11
Prov-Gigapath	brain	<u>0.092</u> (0.073–0.110)	24	11
Phikon-v2	brain	0.098 (0.079–0.118)	24	11
H-optimus-1	brain	<u>0.099</u> (0.072–0.126)	24	11
Shazam	brain	<b>0.136</b> <b>(0.102–0.171)</b>	24	11
UNI 2	bladder	0.053 (-0.004–0.110)	6	5
Virchow2	bladder	<u>0.065</u> <b>(0.008–0.121)</b>	6	5
H-optimus-1	bladder	0.035 (-0.028–0.099)	6	5
Prov-Gigapath	bladder	0.053 (0.006–0.101)	6	5
Phikon-v2	bladder	0.050 (-0.018–0.119)	6	5
Shazam	bladder	<b>0.115</b> <b>(0.022–0.207)</b>	6	5

Supplementary Table 4: **Performance of Survival Analysis on TCGA-BLCA, TCGA-BRCA, and TCGA-CESC Datasets.** The 95% CI is included in parentheses. The best and second-best performed models are **bolded** and underlined.

Model	TCGA-BLCA	TCGA-BRCA	TCGA-CESC
UNI 2	0.598 (0.526–0.669)	0.627 (0.569–0.685)	0.581 (0.406–0.756)
Virchow2	<u>0.561</u> (0.485–0.637)	0.622 (0.557–0.688)	<u>0.672</u> (0.606–0.738)
H-optimus-1	<u>0.599</u> (0.573–0.624)	0.640 (0.592–0.688)	<b>0.690</b> <b>(0.649–0.731)</b>
Prov-Gigapath	<u>0.539</u> (0.498–0.580)	0.631 (0.543–0.718)	0.631 (0.540–0.722)
Phikon-v2	0.583 (0.506–0.659)	<u>0.662</u> (0.563–0.760)	0.473 (0.312–0.633)
Shazam	<b>0.608</b> <b>(0.555–0.662)</b>	<b>0.670</b> <b>(0.585–0.754)</b>	0.666 (0.606–0.727)

Supplementary Table 5: **Performance of Survival Analysis on TCGA-COADREAD, TCGA-GBMLGG, and TCGA-KIRC Datasets.** The 95% CI is included in parentheses. The best and second-best performed models are **bolded** and underlined.

Model	TCGA-COADREAD	TCGA-GBMLGG	TCGA-KIRC
UNI 2	0.596 (0.540–0.652)	0.756 (0.715–0.797)	0.687 (0.605–0.769)
Virchow2	0.625 (0.558–0.691)	0.756 (0.708–0.805)	0.694 (0.638–0.750)
H-optimus-1	<u>0.646 (0.559–0.732)</u>	<u>0.767 (0.729–0.804)</u>	<u>0.710 (0.640–0.780)</u>
Prov-Gigapath	0.595 (0.542–0.648)	0.766 (0.724–0.809)	0.689 (0.631–0.747)
Phikon-v2	0.574 (0.516–0.633)	0.748 (0.715–0.782)	0.662 (0.584–0.741)
Shazam	<b>0.710 (0.655–0.765)</b>	<b>0.768 (0.726–0.811)</b>	<b>0.742 (0.683–0.802)</b>

Supplementary Table 6: **Performance of Survival Analysis on TCGA-LUAD, TCGA-LUSC, TCGA-SKCM, and TCGA-STAD Datasets.** The 95% CI is included in parentheses. The best and second-best performed models are **bolded** and underlined.

Model	TCGA-LUAD	TCGA-LUSC	TCGA-SKCM	TCGA-STAD
UNI 2	0.596 (0.493–0.700)	0.521 (0.433–0.609)	0.622 (0.589–0.655)	0.584 (0.512–0.657)
Virchow2	<u>0.612 (0.520–0.705)</u>	0.538 (0.456–0.619)	0.629 (0.590–0.668)	<u>0.605 (0.564–0.647)</u>
H-optimus-1	<u>0.588 (0.476–0.699)</u>	<u>0.545 (0.459–0.630)</u>	<u>0.637 (0.613–0.662)</u>	0.601 (0.554–0.648)
Prov-Gigapath	0.603 (0.474–0.731)	<u>0.525 (0.450–0.599)</u>	<u>0.628 (0.604–0.653)</u>	0.563 (0.517–0.608)
Phikon-v2	0.571 (0.507–0.635)	0.498 (0.416–0.579)	0.581 (0.537–0.625)	0.591 (0.515–0.668)
Shazam	<b>0.628 (0.577–0.679)</b>	<b>0.583 (0.525–0.641)</b>	<b>0.657 (0.613–0.701)</b>	<b>0.626 (0.531–0.721)</b>

Supplementary Table 7: **Tile-level classification performance of different foundation models on HunCRC dataset.** Non-parametric bootstrapping with 1,000 replicates is employed for statistical analysis. The 95% CI is included in parentheses. Best performing model is **bolded** and second-best is underlined.

Model	Balanced ACC	Weighted F1	AUC
UNI 2	0.520 (0.492–0.546)	0.439 (0.421–0.458)	0.812 (0.807–0.817)
Virchow2	<b>0.567 (0.545–0.588)</b>	<u>0.443 (0.427–0.460)</u>	0.797 (0.792–0.802)
H-optimus-1	0.458 (0.435–0.483)	0.414 (0.397–0.430)	0.829 (0.824–0.833)
Prov-Gigapath	0.472 (0.446–0.499)	0.428 (0.408–0.448)	<b>0.833 (0.828–0.838)</b>
Phikon-v2	0.472 (0.446–0.498)	0.409 (0.393–0.426)	0.814 (0.809–0.819)
Shazam	<u>0.549 (0.523–0.575)</u>	<b>0.459 (0.442–0.475)</b>	0.829 (0.824–0.834)

Supplementary Table 8: **Tile-level classification performance of different foundation models on UniToPatho dataset.** Non-parametric bootstrapping with 1,000 replicates is employed for statistical analysis. The 95% CI is included in parentheses. Best performing model is **bolded** and second-best is underlined.

Model	Balanced ACC	Weighted F1	AUC
UNI 2	<u>0.560 (0.539–0.583)</u>	0.536 (0.515–0.558)	0.560 (0.543–0.579)
Virchow2	<b>0.606 (0.584–0.628)</b>	<b>0.586 (0.565–0.608)</b>	<u>0.610 (0.590–0.630)</u>
H-optimus-1	0.465 (0.444–0.486)	0.423 (0.401–0.443)	<u>0.505 (0.486–0.525)</u>
Prov-Gigapath	0.498 (0.479–0.518)	0.508 (0.488–0.529)	0.595 (0.576–0.616)
Phikon-v2	0.540 (0.519–0.562)	0.497 (0.474–0.518)	0.553 (0.534–0.572)
Shazam	0.532 (0.511–0.553)	<u>0.548 (0.525–0.570)</u>	<b>0.622 (0.604–0.643)</b>

Supplementary Table 9: **Tile-level classification performance of different foundation models on PCAM dataset.** Non-parametric bootstrapping with 1,000 replicates is employed for statistical analysis. The 95% CI is included in parentheses. Best performing model is **bolded** and second-best is underlined.

Model	Balanced ACC	Weighted F1	AUC
UNI 2	0.932 (0.929–0.934)	0.932 (0.929–0.934)	0.932 (0.929–0.935)
Virchow2	0.929 (0.927–0.932)	0.929 (0.926–0.932)	0.929 (0.927–0.932)
H-optimus-1	<u>0.935 (0.932–0.938)</u>	<u>0.935 (0.932–0.937)</u>	<u>0.935 (0.932–0.938)</u>
Prov-Gigapath	<u>0.930 (0.927–0.932)</u>	<u>0.929 (0.927–0.932)</u>	0.930 (0.927–0.932)
Phikon-v2	0.886 (0.882–0.889)	0.885 (0.881–0.888)	0.886 (0.882–0.889)
Shazam	<b>0.944 (0.942–0.947)</b>	<b>0.944 (0.941–0.947)</b>	<b>0.944 (0.941–0.947)</b>

Supplementary Table 10: **Tile-level classification performance of different foundation models on ESCA dataset.** Non-parametric bootstrapping with 1,000 replicates is employed for statistical analysis. The 95% CI is included in parentheses. Best performing model is **bolded** and second-best is underlined.

Model	Balanced ACC	Weighted F1	AUC
UNI 2	0.808 (0.803–0.813)	0.832 (0.827–0.836)	0.945 (0.944–0.946)
Virchow2	<u>0.848 (0.843–0.853)</u>	<u>0.867 (0.863–0.871)</u>	<b>0.956 (0.955–0.957)</b>
H-optimus-1	0.812 (0.807–0.817)	0.837 (0.833–0.842)	0.951 (0.950–0.952)
Prov-Gigapath	0.782 (0.778–0.787)	0.787 (0.782–0.791)	0.921 (0.919–0.922)
Phikon-v2	0.762 (0.757–0.767)	0.736 (0.730–0.740)	0.879 (0.878–0.881)
Shazam	<b>0.868 (0.863–0.873)</b>	<b>0.881 (0.878–0.885)</b>	<u>0.953 (0.952–0.954)</u>

Supplementary Table 11: **Tile-level classification performance of different foundation models on PanCancer-TIL dataset.** Non-parametric bootstrapping with 1,000 replicates is employed for statistical analysis. The 95% CI is included in parentheses. Best performing model is **bolded** and second-best is underlined.

Model	Balanced ACC	Weighted F1	AUC
UNI 2	<b>0.918 (0.915–0.921)</b>	0.908 (0.905–0.911)	0.943 (0.941–0.945)
Virchow2	0.902 (0.898–0.906)	<u>0.910 (0.907–0.913)</u>	<b>0.946 (0.945–0.948)</b>
H-optimus-1	0.912 (0.908–0.915)	0.902 (0.899–0.905)	0.939 (0.937–0.941)
Prov-Gigapath	0.908 (0.904–0.911)	0.898 (0.895–0.901)	0.937 (0.935–0.938)
Phikon-v2	0.913 (0.910–0.916)	0.909 (0.906–0.912)	0.944 (0.942–0.946)
Shazam	<u>0.916 (0.912–0.919)</u>	<b>0.912 (0.909–0.915)</b>	<u>0.946 (0.944–0.948)</u>

Supplementary Table 12: **Tile-level classification performance of different foundation models on CRC-100k dataset.** Non-parametric bootstrapping with 1,000 replicates is employed for statistical analysis. The 95% CI is included in parentheses. Best performing model is **bolded** and second-best is underlined.

Model	Balanced ACC	Weighted F1	AUC
UNI 2	<u>0.953 (0.947–0.958)</u>	0.949 (0.943–0.954)	0.960 (0.956–0.964)
Virchow2	<u>0.953 (0.947–0.958)</u>	0.948 (0.941–0.954)	<u>0.967 (0.962–0.971)</u>
H-optimus-1	0.952 (0.946–0.957)	0.946 (0.939–0.953)	0.965 (0.961–0.970)
Prov-Gigapath	0.952 (0.946–0.957)	0.948 (0.943–0.954)	0.964 (0.959–0.969)
Phikon-v2	0.928 (0.922–0.935)	0.925 (0.918–0.932)	0.950 (0.945–0.954)
Shazam	<b>0.960 (0.955–0.966)</b>	<b>0.956 (0.949–0.962)</b>	<b>0.972 (0.968–0.977)</b>

Supplementary Table 13: **Tile-level classification performance of different foundation models on CCRCC dataset.** Non-parametric bootstrapping with 1,000 replicates is employed for statistical analysis. The 95% CI is included in parentheses. Best performing model is **bolded** and second-best is underlined.

Model	Balanced ACC	Weighted F1	AUC
UNI 2	0.964 (0.954–0.972)	0.960 (0.952–0.967)	0.974 (0.970–0.979)
Virchow2	<u>0.964 (0.955–0.972)</u>	0.961 (0.952–0.968)	0.972 (0.968–0.976)
H-optimus-1	0.960 (0.951–0.968)	0.957 (0.949–0.965)	0.972 (0.968–0.976)
Prov-Gigapath	0.958 (0.949–0.967)	0.959 (0.951–0.966)	0.971 (0.966–0.975)
Phikon-v2	<b>0.965 (0.957–0.973)</b>	0.959 (0.950–0.967)	0.973 (0.968–0.977)
Shazam	0.963 (0.953–0.971)	<b>0.966 (0.959–0.973)</b>	<b>0.975 (0.971–0.979)</b>

Supplementary Table 14: **Tile-level classification performance of different foundation models on BACH dataset.** Non-parametric bootstrapping with 1,000 replicates is employed for statistical analysis. The 95% CI is included in parentheses. Best performing model is **bolded** and second-best is underlined.

Model	Balanced ACC	Weighted F1	AUC
UNI 2	<b>0.988 (0.958–1.000)</b>	<b>0.987 (0.958–1.000)</b>	<b>0.988 (0.963–1.000)</b>
Virchow2	<b>0.988 (0.958–1.000)</b>	<b>0.987 (0.958–1.000)</b>	<b>0.988 (0.963–1.000)</b>
H-optimus-1	<u>0.963 (0.916–1.000)</u>	<u>0.962 (0.913–1.000)</u>	<u>0.963 (0.912–1.000)</u>
Prov-Gigapath	0.912 (0.844–0.969)	0.915 (0.848–0.972)	0.912 (0.850–0.975)
Phikon-v2	0.825 (0.738–0.901)	0.829 (0.741–0.905)	0.825 (0.738–0.900)
Shazam	<b>0.988 (0.958–1.000)</b>	<b>0.987 (0.958–1.000)</b>	<b>0.988 (0.963–1.000)</b>

Supplementary Table 15: **Tile-level classification performance of different foundation models on CRC-MSI dataset.** Non-parametric bootstrapping with 1,000 replicates is employed for statistical analysis. The 95% CI is included in parentheses. Best performing model is **bolded** and second-best is underlined.

Model	Balanced ACC	Weighted F1	AUC
UNI 2	<u>0.736 (0.729–0.743)</u>	0.713 (0.707–0.719)	0.829 (0.826–0.834)
Virchow2	<u>0.733 (0.726–0.740)</u>	0.722 (0.715–0.728)	<u>0.842 (0.838–0.846)</u>
H-optimus-1	0.721 (0.714–0.728)	<u>0.700 (0.694–0.706)</u>	<u>0.822 (0.818–0.826)</u>
Prov-Gigapath	0.730 (0.723–0.737)	0.693 (0.687–0.699)	0.806 (0.802–0.810)
Phikon-v2	0.633 (0.626–0.640)	0.633 (0.626–0.639)	0.801 (0.796–0.805)
Shazam	<b>0.738 (0.731–0.745)</b>	<b>0.726 (0.720–0.732)</b>	<b>0.844 (0.840–0.848)</b>

Supplementary Table 16: **Tile-level classification performance of different foundation models on PanCancer-TCGA dataset.** Non-parametric bootstrapping with 1,000 replicates is employed for statistical analysis. The 95% CI is included in parentheses. Best performing model is **bolded** and second-best is underlined.

Model	Balanced ACC	Weighted F1	AUC
UNI 2	0.919 (0.916–0.922)	0.925 (0.922–0.927)	0.938 (0.936–0.940)
Virchow2	<u>0.914 (0.911–0.917)</u>	0.920 (0.917–0.923)	0.934 (0.933–0.936)
H-optimus-1	<u>0.927 (0.924–0.930)</u>	<b>0.932 (0.930–0.935)</b>	<b>0.946 (0.945–0.948)</b>
Prov-Gigapath	0.909 (0.906–0.912)	0.913 (0.910–0.916)	0.930 (0.929–0.932)
Phikon-v2	0.909 (0.905–0.912)	0.916 (0.913–0.918)	0.929 (0.928–0.931)
Shazam	<b>0.928 (0.925–0.930)</b>	<u>0.931 (0.929–0.934)</u>	0.945 (0.944–0.947)

Supplementary Table 17: **Tile-level classification performance of different foundation models on Chaoyang dataset.** Non-parametric bootstrapping with 1,000 replicates is employed for statistical analysis. The 95% CI is included in parentheses. Best performing model is **bolded** and second-best is underlined.

Model	Balanced ACC	Weighted F1	AUC
UNI 2	0.767 (0.745–0.787)	0.767 (0.745–0.784)	0.820 (0.802–0.833)
Virchow2	<u>0.821 (0.802–0.840)</u>	<b>0.823 (0.805–0.841)</b>	<b>0.868 (0.853–0.881)</b>
H-optimus-1	0.801 (0.780–0.820)	0.798 (0.780–0.817)	0.842 (0.826–0.858)
Prov-Gigapath	0.786 (0.765–0.807)	0.791 (0.771–0.810)	0.842 (0.825–0.856)
Phikon-v2	0.765 (0.744–0.785)	0.776 (0.754–0.795)	0.834 (0.816–0.849)
Shazam	<b>0.824 (0.805–0.844)</b>	<u>0.820 (0.800–0.838)</u>	<u>0.862 (0.846–0.876)</u>

Supplementary Table 18: **VQA Performance on the PathVQA Dataset.** The 95% CI is included in parentheses. The best and second-best performed models are **bolded** and underlined.

Model	Top-1 ACC
UNI 2	<u>0.565 (0.554–0.578)</u>
Virchow2	<u>0.559 (0.547–0.571)</u>
H-optimus-1	0.551 (0.539–0.563)
Prov-Gigapath	0.562 (0.550–0.574)
Phikon-v2	0.532 (0.520–0.545)
Shazam	<b>0.575 (0.563–0.587)</b>

## References

1. Van der Laak, J., Litjens, G. & Ciompi, F. Deep learning in histopathology: the path to the clinic. *Nature medicine* **27**, 775–784 (2021).
2. Shmatko, A., Ghaffari Laleh, N., Gerstung, M. & Kather, J. N. Artificial intelligence in histopathology: enhancing cancer research and clinical oncology. *Nature cancer* **3**, 1026–1038 (2022).
3. Vorontsov, E. *et al.* A foundation model for clinical-grade computational pathology and rare cancers detection. *Nature medicine* **30**, 2924–2935 (2024).
4. Chen, R. J. *et al.* Towards a general-purpose foundation model for computational pathology. *Nature medicine* **30**, 850–862 (2024).
5. Bioptimus. H-optimus-1 (2025). URL <https://huggingface.co/bioptimus/H-optimus-1>.
6. Campanella, G. *et al.* A clinical benchmark of public self-supervised pathology foundation models. *Nature Communications* **16**, 3640 (2025).
7. Neidlinger, P. *et al.* Benchmarking foundation models as feature extractors for weakly supervised computational pathology. *Nature Biomedical Engineering* 1–11 (2025).
8. Ma, J. *et al.* Pathbench: A comprehensive comparison benchmark for pathology foundation models towards precision oncology. *arXiv preprint arXiv:2505.20202* (2025).
9. Xu, H. *et al.* A whole-slide foundation model for digital pathology from real-world data. *Nature* **630**, 181–188 (2024).
10. Deng, J. *et al.* Imagenet: A large-scale hierarchical image database. In *2009 IEEE conference on computer vision and pattern recognition*, 248–255 (Ieee, 2009).
11. Schuhmann, C. *et al.* Laion-5b: An open large-scale dataset for training next generation image-text models. *Advances in neural information processing systems* **35**, 25278–25294 (2022).
12. Amazon Web Services. Common crawl dataset. <https://registry.opendata.aws/commoncrawl/>.
13. Ma, J. *et al.* A generalizable pathology foundation model using a unified knowledge distillation pretraining framework. *Nature Biomedical Engineering* 1–20 (2025).
14. Fang, L. *et al.* Knowledge distillation and dataset distillation of large language models: Emerging trends, challenges, and future directions. *Artificial Intelligence Review* **59**, 17 (2026).
15. Fedus, W., Zoph, B. & Shazeer, N. Switch transformers: Scaling to trillion parameter models with simple and efficient sparsity. *Journal of Machine Learning Research* **23**, 1–39 (2022).
16. Zimmermann, E. *et al.* Virchow2: Scaling self-supervised mixed magnification models in pathology. *arXiv preprint arXiv:2408.00738* (2024).
17. Filiot, A., Jacob, P., Kain, A. M. & Saillard, C. Phikon-v2, a large and public feature extractor for biomarker prediction (2024). URL <https://arxiv.org/abs/2409.09173>.
18. Ståhl, P. L. *et al.* Visualization and analysis of gene expression in tissue sections by spatial transcriptomics. *Science* **353**, 78–82 (2016).
19. Baccin, C. *et al.* Combined single-cell and spatial transcriptomics reveal the molecular, cellular and spatial bone marrow niche organization. *Nature cell biology* **22**, 38–48 (2020).

20. Janesick, A. *et al.* High resolution mapping of the tumor microenvironment using integrated single-cell, spatial and *in situ* analysis. *Nature communications* **14**, 8353 (2023).
21. Meylan, M. *et al.* Tertiary lymphoid structures generate and propagate anti-tumor antibody-producing plasma cells in renal cell cancer. *Immunity* **55**, 527–541 (2022).
22. Bassiouni, R. *et al.* Spatial transcriptomic analysis of a diverse patient cohort reveals a conserved architecture in triple-negative breast cancer. *Cancer research* **83**, 34–48 (2023).
23. Parigi, S. M. *et al.* The spatial transcriptomic landscape of the healing mouse intestine following damage. *Nature communications* **13**, 828 (2022).
24. Jaume, G. *et al.* Hest-1k: A dataset for spatial transcriptomics and histology image analysis. In *Advances in Neural Information Processing Systems* (2024).
25. Amin, M. B. *et al.* The eighth edition ajcc cancer staging manual: continuing to build a bridge from a population-based to a more “personalized” approach to cancer staging. *CA: a cancer journal for clinicians* **67**, 93–99 (2017).
26. Weinstein, J. N. *et al.* The cancer genome atlas pan-cancer analysis project. *Nature genetics* **45**, 1113–1120 (2013).
27. El Nahhas, O. S. *et al.* From whole-slide image to biomarker prediction: end-to-end weakly supervised deep learning in computational pathology. *Nature protocols* **20**, 293–316 (2025).
28. Pataki, B. Á. *et al.* Huncrc: annotated pathological slides to enhance deep learning applications in colorectal cancer screening. *Scientific Data* **9**, 370 (2022).
29. Barbano, C. A. *et al.* Unitopatho, a labeled histopathological dataset for colorectal polyps classification and adenoma dysplasia grading. In *2021 IEEE International Conference on Image Processing (ICIP)*, 76–80 (IEEE, 2021).
30. Bejnordi, B. E. *et al.* Diagnostic assessment of deep learning algorithms for detection of lymph node metastases in women with breast cancer. *JAMA* **318**, 2199–2210 (2017).
31. Tolkach, Y. Datasets for Publication ”Artificial intelligence for tumor detection and histological regression grading in oesophageal adenocarcinomas: a retrospective algorithm development and validation study” Tolkach Y. *et al.* (2023). URL <https://doi.org/10.5281/zenodo.7548828>.
32. Saltz, J. *et al.* Spatial organization and molecular correlation of tumor-infiltrating lymphocytes using deep learning on pathology images. *Cell reports* **23**, 181–193 (2018).
33. Brummer, O., Pölönen, P., Mustjoki, S. & Brück, O. Computational textural mapping harmonises sampling variation and reveals multidimensional histopathological fingerprints. *British Journal of Cancer* **129**, 683–695 (2023).
34. Aresta, G. *et al.* Bach: Grand challenge on breast cancer histology images. *Medical image analysis* **56**, 122–139 (2019).
35. Kather, J. N. *et al.* Deep learning can predict microsatellite instability directly from histology in gastrointestinal cancer. *Nature medicine* **25**, 1054–1056 (2019).
36. Komura, D. *et al.* Universal encoding of pan-cancer histology by deep texture representations. *Cell Reports* **38** (2022).
37. Zhu, C., Chen, W., Peng, T., Wang, Y. & Jin, M. Hard sample aware noise robust learning for histopathology image classification. *IEEE transactions on medical imaging* **41**, 881–894 (2021).

38. He, X., Zhang, Y., Mou, L., Xing, E. & Xie, P. Pathvqa: 30000+ questions for medical visual question answering. *arXiv preprint arXiv:2003.10286* (2020).
39. Filot, A. *et al.* Distilling foundation models for robust and efficient models in digital pathology. In *International Conference on Medical Image Computing and Computer-Assisted Intervention*, 162–172 (Springer, 2025).
40. Ilse, M., Tomczak, J. & Welling, M. Attention-based deep multiple instance learning. In *Proceedings of the 35th International Conference on Machine Learning*, 2132–2141 (2018).
41. Piñeiro, A. J., Houser, A. E. & Ji, A. L. Research techniques made simple: spatial transcriptomics. *Journal of investigative dermatology* **142**, 993–1001 (2022).
42. OncoKB. Oncokb: Fda recognition. <https://www.oncokb.org/fda-recognition> (2024). Accessed: 2025-12-05.
43. Veeling, B. S., Linmans, J., Winkens, J., Cohen, T. & Welling, M. Rotation equivariant cnns for digital pathology. In *International Conference on Medical image computing and computer-assisted intervention*, 210–218 (Springer, 2018).
44. Tolkach, Y. *et al.* Artificial intelligence for tumour tissue detection and histological regression grading in oesophageal adenocarcinomas: a retrospective algorithm development and validation study. *The Lancet Digital Health* **5**, e265–e275 (2023).
45. Kather, J. N. *et al.* Predicting survival from colorectal cancer histology slides using deep learning: A retrospective multicenter study. *PLoS medicine* **16**, e1002730 (2019).
46. Lu, M. Y. *et al.* Data efficient and weakly supervised computational pathology on whole slide images. *Nature Biomedical Engineering* (2020).
47. Ma, J. *et al.* Towards a generalizable pathology foundation model via unified knowledge distillation. *arXiv preprint arXiv:2407.18449* (2024).
48. Weinstein, J. N. *et al.* The cancer genome atlas pan-cancer analysis project. *Nature genetics* **45**, 1113–1120 (2013).
49. Li, P., Liu, G., He, J., Zhao, Z. & Zhong, S. Masked vision and language pre-training with unimodal and multimodal contrastive losses for medical visual question answering. In *International Conference on Medical Image Computing and Computer-Assisted Intervention*, 374–383 (Springer, 2023).